We are IntechOpen,
the world's leading publisher of
Open Access books
Built by scientists, for scientists

6,900
Open access books available

186,000
International authors and editors

200M
Downloads

Our authors are among the

154
Countries delivered to

TOP 1%
most cited scientists

12.2%
Contributors from top 500 universities

CLARIVATE ANALYTICS
BOOK
CITATION
INDEX
INDEXED

WEB OF SCIENCE™

Selection of our books indexed in the Book Citation Index
in Web of Science™ Core Collection (BKCI)

Interested in publishing with us?
Contact book.department@intechopen.com

Nanostructure, Texture Evolution and Mechanical Properties of Aluminum Alloys Processed by Severe Plastic Deformation

Abbas Akbarzadeh
Department of Materials Science and Engineering, Sharif University of Technology,
Tehran,
Iran

1. Introduction

Various research works have been conducted to replace heavy steel body constructions with lighter aluminum ones to achieve stronger energy consumption and environmental standards. The most important technical obstacle to this goal is the inferior ductility of most aluminum sheet alloys. It has been reported that control of the microstructure and the texture of materials is essential for improvement of their mechanical properties (Lee et al., 2002). Reducing the grain size of polycrystalline metallic materials to the nanosize ($d < 100$ nm, nanocrystalline) or submicron levels (100 nm$< d <$1 µm, ultra-fine grain) is an effective and relatively economic way of improving mechanical properties such as strength, toughness, or wear resistance in structural materials (Kim et al., 2006; Prangnell et al., 2001) which even can give rise to superplastic behavior under appropriate loading conditions (Pérez-Prado et al., 2004). Since it is practically difficult to reduce the grain size of many metallic materials such as aluminum alloys below 5 µm by a conventional cold working and recrystallization process, several new methods are developed to manufacture ultrafine grained (UFG) materials (Kim et al., 2006). These methods can be classified into two main groups namely bottom-up and top-down processes. In the bottom-up procedures, such as rapid solidification, vapor deposition and mechanical alloying, an ultra-fine microstructures is configured from the smallest possible constituents which are prohibited to grow into the micrometer domain (Pérez-Prado et al., 2004). In the top-down procedures, on the other hand, an existing microscale microstructure is refined to the submicrometer scale, e.g. by a process such as severe plastic deformation (SPD) (Pérez-Prado et al., 2004; Saito et al., 1999). The ancient Persian swords are the interesting examples of severe upset forging for development of fine microstructures (Sherby and Wadsworth, 2001).

By now, various SPD processes such as accumulative roll bonding (ARB) (Saito et al., 1999), cyclic extrusion compression (CEC) (Richert J. & Richert M., 1986), equal channel angular pressing (ECAP) (Valiev et al., 1991), and high pressure torsion (HPT) (Horita et al., 1996) have been proposed and successfully applied to various materials. The common feature of these techniques is that the net shape of the sample during processing is approximately constant, so that there is no geometric limitation on the applied strain (Prangnell et al., 2001). Among these processes, accumulative roll bonding has some unique features. Firstly,

unlike the ECAP, CEC and HPT processes which require forming machines with large capacity and expensive dies, the ARB process can be performed by a conventional rolling mill without any special die. Secondly, in comparison to the other methods, the productivity of the ARB process is relatively high because this process implies the potential of industrial up scaling to a continuous production of UFGed metallic sheets or plates (Saito et al., 1999). In principle at least, the use of heavy deformation in metal processing, with the objective of producing metal alloys with superior properties, has a long history which may be traced back to the early metal-working of ancient China [16], the blacksmith's production of high-quality Damascus steel in the Middle East [17] and the fabrication of the legendary Wootz steel in ancient India [18].

The ARB process is a repetitive procedure of cutting, stacking and roll bonding of similar sheets for a desired number of cycles, Fig. 1, which is practically limited by technological constraints such as the occurrence of edge cracks. In this process the thickness of the sheet varies between fixed limits and by repeating the procedure very high strains can be accumulated in material, and as a result significant structural refinement can be achieved (Huang et al., 2003; Saito et al., 1999; Tsuji et al., 2003a).
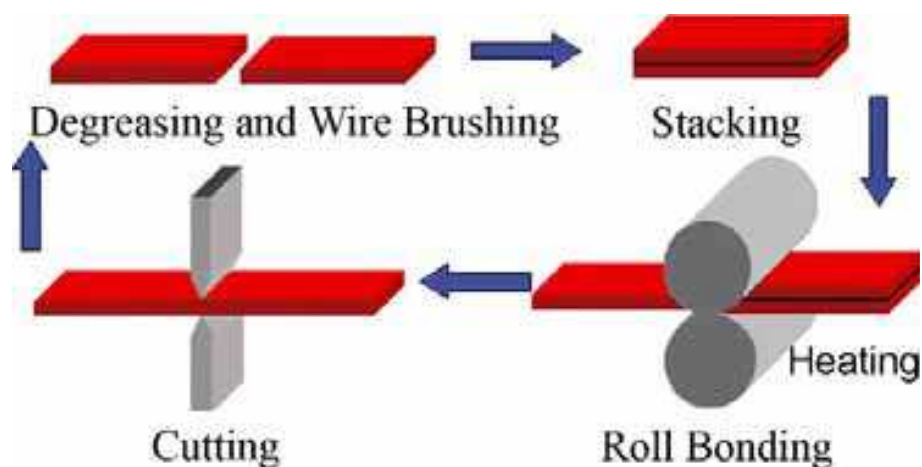

Fig. 1. Schematic illustration showing the procedure of the ARB process (Pirgazi et al., 2008a)

The first scientific paper on the ARB was published in 1998 and afterwards extensive studies have been conducted regarding the microstructural evolution and mechanical properties of various materials processed in different ARB cycles. Pure aluminum (Huang et al., 2003; Saito et al., 1998; Tsuji et al., 2003a), AA5083 (Saito et al., 1999), AA6061 (Lee et al., 2002; Park et al., 2001), AA8011 (Kim et al., 2002, 2005), AA3103 (Chowdhury et al., 2006a) and AA8090 (Chowdhury et al., 2006b) aluminum alloys, magnesium alloys (del Valle et al., 2005; Pérez-Prado et al., 2004), and Ti-IF steel sheets (Reis & Kestens, 2005, Reis et al., 2005; Tsuji et al., 2002a) are the most important materials which have already been successfully produced by the ARB process. The results of these investigations mainly indicate that during the first stages of ARB, ultra-fine grains with diameter less than 1 μm partially form in the sheets, and the volume fraction of these grains increases with increasing the number of cycles, so that after high levels of strain the sample is completely covered with ultra-fine lamellar grains which are not equi-axed and represent an aspect ratio bigger than one (Huang et al., 2003; Park et al., 2001; Saito et al., 1998; Tsuji et al., 2003a). The investigations on the mechanical properties by previous researchers show that the ARB is a promising process for improving this feature of metallic sheets. It has been reported that a significant

increase in strength and hardness, more than two or three times of the values of starting materials can be achieved by ARB process in aluminum alloys and IF steel sheets (Lee et al., 2004; Park et al., 2001; Saito et al., 1998; Tsuji et al, 2002b).

Microstructural evolution during ARB has been studied by several researchers. TEM investigation and local crystallography were used (Huang et al., 2003) to study the microstructural evolution of AA1100 up to eight cycles of ARB. Their results show that at large strains, almost a homogenous lamellar structure is formed across the thickness. This microstructure is subdivided by high angle boundaries and low angle dislocation boundaries. The spacing of dislocation boundaries decrease and their misorientations increase by accumulating strain. EBSD analysis illustrates three mechanisms of UFGs development at different levels of strains (Pirgazi et al., 2008b). It was shown that development of subgrains is the major mechanism during the first two cycles of ARB. This mechanism is followed by strain induced transition of low angle grain boundaries to high angles and formation of a thin lamellar structure at medium levels of strain. Fragmentation of these thin lamellar structures into more equi-axed grains is considered as the dominant mechanism after sixth cycle of ARB. A similar microstructural evolution during ARB of AA6061 has been reported (Park et al., 2001). In addition to fabrication of UFGed and nanostructured materials for metallic sheets, some other unique features for ARB process are applied to different sheets to fabricate multi-layer composites (Min et al., 2006).

The texture analysis is a powerful tool to investigate the microstructural and substructural evolution of plastically deformed materials because it provides information on the fragmentation behavior of grains. When orientation contrast microscopy is used, the microstructural data can be linked with local textural information. It is commonly known that in materials produced by severe plastic deformation processes, the band contrast of the corresponding Kikuchi-lines decreases as a result of the presence of lattice defects, such as regions with high dislocation density, subgrains and grain boundaries. In the TSL® software, the contrast of the Kikuchi lines is quantified by the image quality (IQ) parameter. The IQ parameter is sensitive to a wide variety of additional material and instrumental factors which makes it almost impossible to deconvolute the IQ signal in order to convert it to univocal quantitative information on the local microstrain. Nevertheless, the EBSD technique is the only possible tool for nanoscale analysis of relatively large areas in severely deformed materials at present (Tsuji et al., 2002a).

It has been reported (Chowdhury et al., 2006a) that the texture development in an AA3103 alloy during accumulative roll bonding process shows symmetry at all stages and the major components can be characterized as the Dillamore {4411} <11 11 8> component along with the S component with a scatter around the brass component. It has been also reported that in AA8011 aluminum alloy sheets processed by ARB, the deformation texture is dominated by the Dillamore component and the shear texture was developed near the surface of the sheets. This surface shear texture disappears rapidly as the surface area of the material re-appears in the center of the composite sample in the next ARB pass (Kim et al, 2002, 2005). Similar results have been published by (Heason & Prangnell, 2002a). They have reported that in AA1100 alloy processed by the ARB, coarse unrefined bands can be retained even at very high strains. They have also proposed that the strong texture developed during ARB processing may lead to this inhomogeneity (Heason & Prangnell, 2002a). It has also been reported that the textures in Ti-IF steel produced by ARB display a conventional cross sectional gradient with typical shear component in the subsurface planes and plane strain compression components in the midsection (Reis & Kestens, 2005; Kolahi et al., 2009).

It has been reported that in AA8011 aluminium alloy sheets processed by ARB, the main deformation texture orientation is the Dillamore {4 4 11}<11 11 8> component and the shear texture is developed on the surface of the sheets (Kim et al., 2002). This surface shear texture disappears rapidly as the surface area of the material reappears in the centre of the composite sample during the next ARB cycle. The role of second phase particles on the grain size reduction of aluminium sheets during the accumulative roll bonding process has been investigated by comparing the microstructure and texture of a single phase (AA1100) and a particle containing aluminium alloy (AA3003) during various ARB cycles (Pirgazi & Akbarzadeh, 2009).

Circular shaped hollow sections like tubes and cylinders, as a category of engineering components, are also expected to achieve high strengths by nanostructure. Tube spinning is used as a common tube fabricating process (Wong et al., 2003), based on which a cold-bonding process titled "spin-bonding" with the advantages of ARB of sheets has been recently proposed (Mohebbi & Akbarzadeh, 2010a, 2010b) for manufacturing of high strength thin-walled tubes and cylinders. The SPD process proposed in that work is, in fact, repeatedly spin-bonding of layered tubes (accumulative spin-bonding, ASB) to induce large plastic strain on tubes similar to the ARB of sheets, Fig. 2 (Mohebbi & Akbarzadeh, 2010a).
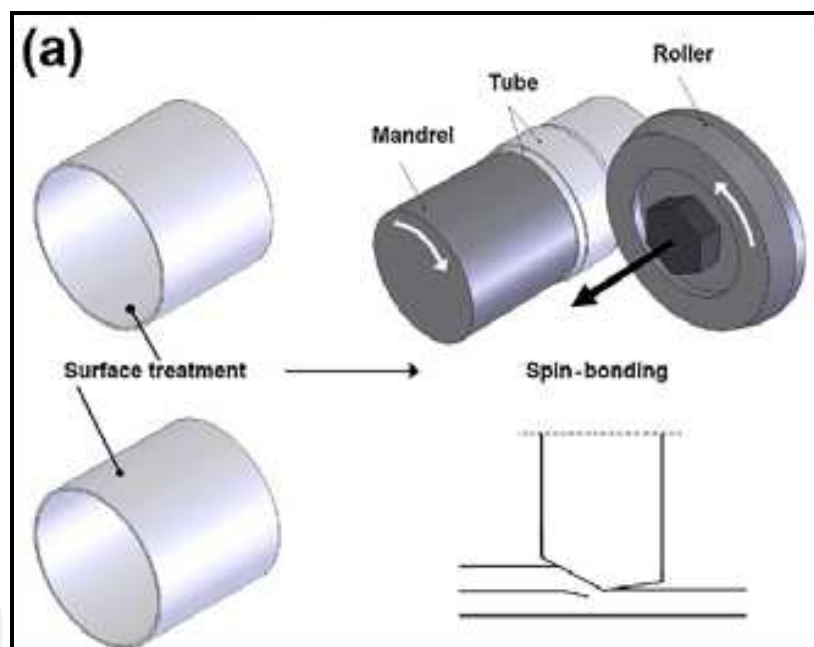

Fig. 2. Schematic illustration of the spin-bonding (Mohebbi & Akbarzadeh, 2010a)

In many cases, the inner and outer surfaces of hollow sections are exposed to different environments, and different characteristics are required inside and outside. In these cases, various bimetallic or clad tubes of stainless steels or high-alloy steels and super alloys clad onto carbon or low alloy steels, are utilized in boilers, heat exchangers, nuclear power plants and petroleum and chemical industries (Chen et al., 2003). So far, several methods have been used to produce composite tubes and cylinders. While centrifugal casting (Sponseller et al., 1998) and extrusion (Chen et al., 2003) can be used to fabricate the thick-walled bimetallic tubes, explosive bonding (Berski et al., 2006), ball attrition (Zhan et al., 2006), thermo-hydraulic fit method and hydraulic expansion method (Wang et al., 2005) are capable of manufacturing thin-walled cylinders. The most widely used cladding process is roll-

bonding of two or more sandwich sheets (Zhan et al., 2006). Although it is possible to fabricate seamed composite tubes by sandwich sheets, it is ideal to plan a method with advantages of roll-bonding to produce seamless thin-walled tubes and cylinders. The spin-bonding method in cold-bonding of cylinders was also proposed by utilizing the tube spinning process for manufacturing of clad tubes (Mohebbi, 2009a).

Tube spinning is an incremental and localized deformation in which material between the roller and the mandrel gradually deforms to the final thickness. Actually the deformation area is limited to a part of work piece which is in contact to the roller, so that the deformation is constrained strongly by surrounding metals. This is why the stress and strain have such a complicated distribution in this incremental process. There is always an inhomogeneous material flow due to the local deformation between the roller and the preform surface with a high strain rate (Mohebbi & Akbarzadeh, 2010b, 2010c, 2009b).

2. Experimental methods

The materials used to study the ARB process were fully annealed sheets of Al-Mn alloy (AA3003) and commercial purity aluminum (AA1100) with initial grain sizes of 40 and 34 μm. Thickness of the sheets was respectively 0.4 and 0.5 mm, and the chemical compositions are presented in Table 1. Two sheets of 150×50 mm2 were degreased (in acetone) and wire brushed (by a stainless steel brush with wires of 0.4 mm in diameter). After the surface treatment, the two sheets were stacked on top of each other and preheated to a temperature of 250 °C for 5 minutes. The plane strain rolling was performed along the longest dimension by 50% reduction in thickness at 200 °C without any lubrication and the mean strain rate was 51 sec^{-1}. Afterwards the roll bonded sample was cut into two sheets of approximately the initial dimension and the procedure was repeated up to a total of 8 cycles so that an accumulated equivalent strain of 6.4 was achieved.

Alloy	Fe	Cu	Si	Ti	Mg	Mn	Al
AA1100	0.57	0.12	0.13	0.03	0.02	0.013	Bal.
AA3003	0.436	0.216	0.18	0.009	0.005	1.076	Bal.

Table 1. Chemical composition of the aluminium alloys (Pirgazi & Akbarzadeh, 2009)

The microtexture and microstructure measurements were performed on the section which is perpendicular to the transverse direction of rolling and is located at the mid-thickness of the sheets. The analysis was carried out by employing an Orientation Image Microscopy (OIM) attached on a Philips XL30 ESEM microscope equipped with a LaB6 filament. The electron back-scattering diffraction (EBSD) mappings were carried out with step sizes in the range of 0.12 μm to 80 nm and the OIM software developed by TSL® was used for data acquisition and post-processing procedures.

Since the ARBed samples were severely deformed, acquiring good Kikuchi-patterns was not evident. By means of electro polishing a very smooth surface was produced and by adjusting the operating parameters of the SEM and the software (OIM Data Collection) a

satisfying result could be obtained. In this way, after using a grain confidence index (CI) standardization (5°, two points) and neighbor orientation correlation (CI = 0.1) cleanup procedures on the raw data, confidence indices of 0.9 and 0.79 were obtained for the samples processed by 4 and 10 cycles, respectively.

The Vickers micro hardness test was utilized to investigate the mechanical properties of initial and ARB processed samples. The values reported for HV represent the average of ten measurements taken at randomly selected points across the thickness of the sheets using loads of 50 and 100 g for 20 s. The mechanical properties of initial and ARBed samples were measured by tensile tests at room temperature executed with an Instron tensile testing machine. The test specimens were prepared with the tensile axis parallel to the rolling direction. The test conditions and the specimen size were chosen according to the ASTM-E8 standard.

Orientation distribution functions (ODFs) were calculated by harmonic series expansion with truncation at L = 16. The initial texture of the fully annealed AA3003 alloy sheet prior to the ARB process was also characterized using the EBSD analysis. In order to obtain a statistically acceptable result, this measurement was carried out with a step size of 2 µm over an area with dimension of 300 µm×300 µm located at mid thickness and as a result more than 22,000 orientations were analyzed.

The texture evolution during ARB process was predicted with the Alamel model (Van Houtte et al., 2005, 2006). In this model the texture is discretized in a set of N individual orientations which are considered in pairs of two. Each pair of orientations will accommodate the externally imposed strain but shear strains can be relaxed in equal and opposite measure for each grain belonging to a pair. In the ODF calculations the orthorhombic sample symmetry was imposed which is usually assumed for the conventional rolling process. Only the {111} <110> slip systems were taken into account for the texture calculations.

The tubes used for ASB process were prepared from commercially pure aluminum (AA1050). Thickness of the tubes was 0.8 mm. Work pieces were annealed at 350 °C for 2 hrs before the first cycle. Spin-bonding process was repeated up to four cycles. In the spin bonding process two surfaces to be bonded (inner surface of the external tube and outer surface of the internal one) were degreased in acetone and wire brushed as surface treatment. After scratch brushing, surface treated tubes were positioned against each other and fitted on the mandrel for tube spinning at room temperature with conditions of Table 2 (Mohebbi & Akbarzadeh, 2010c). At this stage, while the tube and mandrel rotate about their axes, a roller with a degree of freedom about its own axis moves along the direction of the tube axis to reduce its thickness to 50% leading to bonding of the tubes. No preheating was performed in this work. More details of the spin-bonding is available in (Mohebbi & Akbarzadeh, 2010a).

The longitudinal sections of the specimens were observed by an optical microscope after polishing and etching in the Tucker solution for 15 s. Transmission electron microscopy (TEM) micrographs and the corresponding selected area diffraction (SAD) patterns were also obtained from the specimens after 1, 2 and 4 cycles of ASB. To do so, thin foils were prepared by twin-jet polishing from the mid-thickness of the tubes normal to the tube surface. The microstructural evolution was also analyzed by electron backscattering diffraction (EBSD) pattern. This was performed on the longitudinal sections perpendicular to the peripheral direction of the tubes after various cycles of ASB. The measured area was 25 µm×30 µm located at the center of mid-thickness of the tubes.

Parameter	Value
Workpiece	
Inner diameter (mm)	35
Wall thickness (mm)	2.5
Initial length (mm)	50
Roller	
Diameter (mm)	54
Attack angle (°)	25
Smoothing angle (°)	5
Flow forming conditions	
Feed rate (mm/rev)	0.1
Reduction (%)	40
Speed of rotation (rpm)	30

Table 2. Dimensions of tools and work piece and the process conditions

EBSD patterns were obtained at 25 kV and analyzed by TSL software regarding the quantitative analysis of grain boundaries and misorientation distributions. The step size was 100 nm for the specimens after the first and second cycles and 60 nm for the specimens after the third and fourth cycles of ASB. Mechanical properties of the specimens were determined at ambient temperature with strain rate of 2.6×10^{-3} sec^{-1}. The samples were prepared from the circumferential direction of the tubes after straightening and machining according to the ASTM E8M standard. Vickers microhardness values were also measured through the thickness of the specimens by applying the load of 0.49 N.

The material used in ASB process was the commercial purity aluminum (AA 1050). Thickness of the tubes was 0.8 mm. The inner diameter of the internal tube and the external one were 51 and 52.8 mm, respectively and their length was 40 mm. Work pieces were annealed at 350 °C for 2 hrs before the bonding process. Since they were processed via tube spinning, work pieces were diametrically true after annealing. The bonding surfaces were degreased in acetone and scratch brushed. The time between surface preparation and bonding process was kept to less than 300 s to minimize the formation of contaminant film and a thick oxide layer on the bond surfaces of the tubes. Afterwards, the two tubes to be joined were positioned against each other. The process is schematically illustrated in Fig. 2.

The bond strength of the Al/Al bimetal layers was measured using the T-peel test. Samples were 8 mm wide and 50 mm long and were cut at the longitude of the tubes so that their width was in the circumferential direction. The breaking off force per width of the sample was measured as the bond strength (N/mm). Optical microscopy was employed to examine the bond interface of the longitudinal section of deformation zone. The surfaces to be examined were prepared by standard metallographic procedure to polished conditions without etching.

3. Results and discussions

3.1 Microstructure
3.1.1 ARB processing
Figure 3 shows the optical micrograph observed in the RD-ND section of the sample produced by 10 ARB cycles, indicating that a good bonding with no delamination has been achieved under the present ARB conditions. To investigate the microstructural evolution of

aluminium sheets processed by ARB, the boundary misorientation maps were extracted from the EBSD data. These mappings were recorded on a section near the centre of the RD–ND plane of the samples. Because of the severe deformation of the ARB processed samples, acquiring good Kikuchi-lines was too difficult. However, by means of electropolishing in Barker's reagent (5 mL HBF4 in 200 mL H2O) and preparing a very smooth surface and adjusting the parameters of SEM (e.g. gun high voltage, working distance and spot size) and the OIM Data Collection software (e.g. exposure time, binning and step size), it was significantly improved.
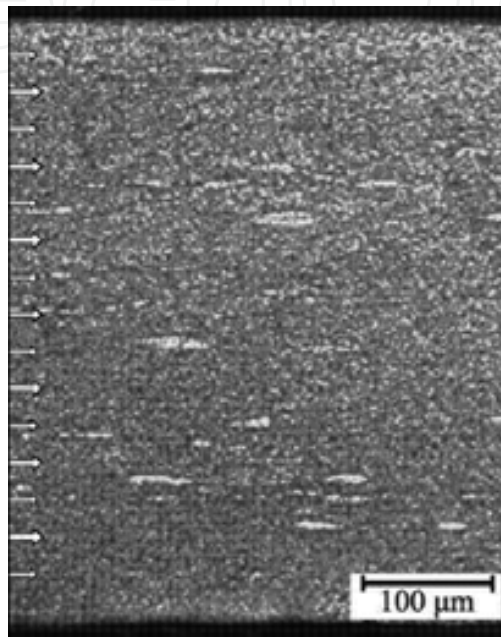
Fig. 3. Optical micrograph of longitudinal cross section of aluminum sheet (AA1100) after 10 ARB cycles

The orientation scans of the AA1100 and AA3003 aluminum sheets processed by various ARB cycles are depicted in Figs. 4 and 5. The boundary misorientation maps of these samples are also depicted in these figures. In these maps, the high angle grain boundaries (HAGB) with misorientations larger than 15° are drawn in bold black lines, while the low angle grain boundaries (LAGB) with misorientations between 2° and 15° are drawn in thin grey lines. In the case of AA1100 alloy, it is observed that after two cycles of ARB, the microstructure is covered with elongated grains surrounded by many low angle grain boundaries (Fig. 4a). The microstructures of the samples produced by four and six ARB cycles are generally similar to the sample produced by two ARB cycles. However, with the increasing number of cycles the grain sizes decrease gradually. After the sixth cycle, the structure consists of very fine elongated grains surrounded by high angle grain boundaries which are usually parallel to the rolling direction (Fig. 4c).

It is observed that the evolution of ultra-fine grains in the AA1100 alloy occurs by various mechanisms of grain refinement at different strains. At low strains ($\varepsilon<1.6$) grain subdivision is the dominant mechanism which leads to the formation of a fibrous microstructure of elongated grains and promotes the formation of subgrains surrounded by a high fraction of low angle grain boundaries (LAGB) (Fig. 4a) and some coarse unrefined bands which contain predominantly subgrains are seen in this specimen. At medium levels of strains

(1.6<ε<4.8) the grain subdivision ratio decreases and strain induced transformation of low angle to high angle grain boundaries (HAGB) caused by the accumulation of dislocations in exiting subgrain boundaries is the controlling mechanism which results in a lamellar structure at the specimens processed by 4 and 6 ARB cycles (Figs. 4b and c). The fraction of HAGB presented in Figs. 4 and 5 confirm the increase of the HAGBs in expense of the LAGBs.

In comparison with the first sample, less pronounced unrefined regions of subgrains are also seen in these samples. The proposed mechanism of grain refinement at high levels of strain (ε>4.8) is the progressive fragmentation of the thin lamellar grains into more equi-axed grain structures which leads to development of a relatively homogeneous submicron grain structure without the unrefined regions after the eighth cycle (Fig. 4d).
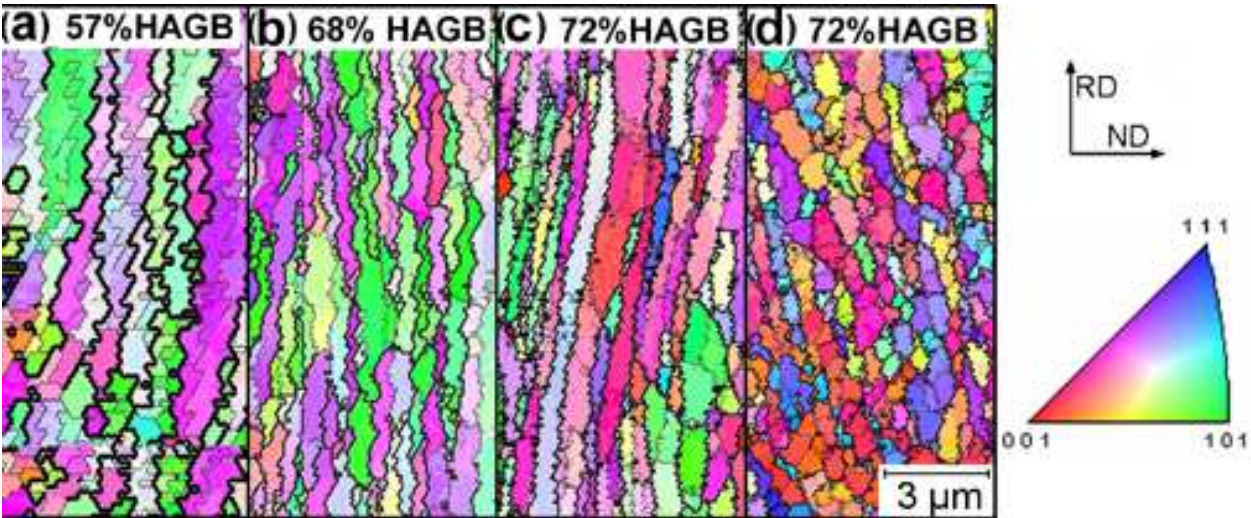
Fig. 4. Orientation scans obtained from the EBSD measurements of the AA1100 ARB processed by (a) 2, (b) 4, (c) 6 and (d) 8 cycles. Thin grey lines represent the misorientation (θ) of 2° ≤θ <15° and bold black lines represent 15° ≤ θ
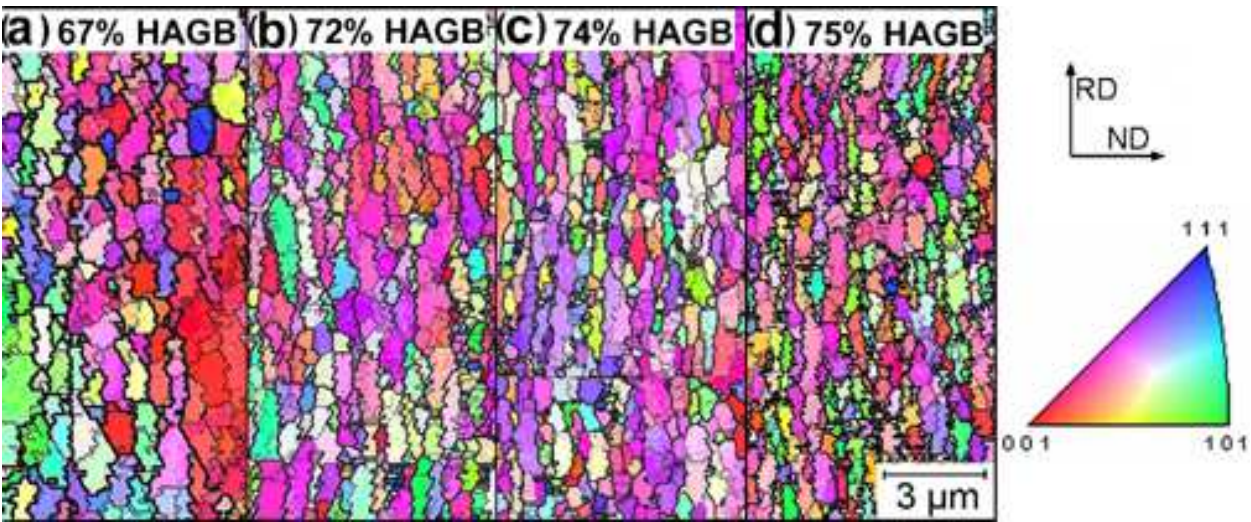
Fig. 5. Orientation scans of the AA3003 samples produced by (a) 2, (b) 4, (c) 6 and (d) 8 ARB cycles

Fig. 5 displays that in comparison with the AA1100 alloy, in the AA3003 alloy which contains a significant volume fraction of second phase particles, an ultra-fine grain structure develops at a much higher rate. It is reported that two types of precipitates evolve in the AA3003 alloy: orthorhombic (Fe,Mn)Al6 and cubic α-Al(Fe,Mn)Si. The total volume fraction of these precipitates is between 4 and 5% and the large majority of them are elongated and have an average length between 1-5 μm (Richert J. & Richert M., 1986). In a similar research on AA8097, it has been shown that these second phase particles cause the texture randomization and promotion of grain refinement (Heason and Prangnell, 2002b).

According to Fig. 5, the volume fraction of HAGBs after the second cycle in the AA3003 alloy is 67% compared to 57% in the AA1100 alloy. This rapid refinement of grains in the AA3003 alloy at relatively low strains results from extensive HAGBs generation in local deformation zones around the second-phase particles. During deformation, large lattice rotation around the second phase particles leads to the increase of local misorientation and production of new HAGBs. Dispersion of these particles also develops a random and more heterogeneous plastic flow behavior within the matrix and promotes the fragmentation of the lamellar structures seen in the AA1100 alloy (Pirgazi & Akbarzadeh, 2008c). This behavior as well as a gradual increase in the percentage of HAGBs and a reduction in the grain aspect ratio during the next cycles results in the formation of a more homogenous submicron grains structure in the AA3003 alloy (Fig. 5).

Although many low angle grain boundaries are also observed in the microstructure, they are usually perpendicular to the rolling direction. Figure 4d displays the microstructure developed in the AA1100 aluminium sheet processed by eight ARB cycles. Significant changes are observed at this level of strain and the grain morphology changes into more equi-axed structures. In comparison with the AA1100 alloy, the developed microstructures in AA3003 alloy during the ARB process are somewhat different. According to Fig. 5, it is clearly observed that in this alloy, the formation of ultrafine grains occurs at the earlier stages of the process. Figure 5a shows that even after the second cycle, the microstructure is completely covered with very fine grains whose morphology is more equi-axed than the same sample of AA1100 alloy (Fig. 4a).

With the number increasing of cycles, the grain size continuously decreases and after the eighth cycle the whole specimen shows a homogenous submicrometre grain size structure. Further analysis revealed that the microstructures of these samples differ in grain size and the fraction of HAGBs. Variations of microstructural parameters of the aluminium sheets during the ARB process are depicted in Fig. 6 with regard to the changes of the average thickness and length of grains. In the AA1100 alloy, the grain thickness (measured by the linear interception method on the EBSD maps) drastically decreases during the first four cycles. While with the increasing strain during the next cycles, the grain thickness reduces slightly and approached to a constant value of about 500 nm at large strains. Similar results are observed in the AA3003 alloy but the grain thickness in this case is smaller than the former case and reaches the minimum of 400 nm after the eighth cycle. Comparison of the grain length in the ARB processed samples revealed that there is a more dramatic difference between the evolved microstructures in the two alloys after a large number of ARB cycles. In the AA3003 alloy, the average length of grains decreases continuously while in the case of AA1100 alloy a drastic reduction is observed after the sixth cycle (Fig. 6b).

By analysing the EBSD data after each ARB cycle, quantitative measurements were made of the misorientation distributions and the results are summarised in Fig. 7. The Mackenzie distribution for boundaries in a random polycrystal is shown by the black bold line. In both

alloys, with ARB processing, the fraction of high angle grain boundaries increases and approaches to a near random misorientation distribution very much similar to the theoretical Mackenzie distribution. However, there are some differences between the misorientation profiles produced in the two alloys during the ARB process. It can be observed that in AA3003 alloy the fraction of HAGBs initially increases rapidly and reaches over 70% after the fourth cycle. During the next cycles, few further changes occur and the fraction of HAGBs after the eighth cycles reaches to 75%. In contrast, the fraction of HAGBs in AA1100 alloy increases more slowly with the increasing strain during the ARB process and reaches a saturation value of about 72% after the sixth cycle.
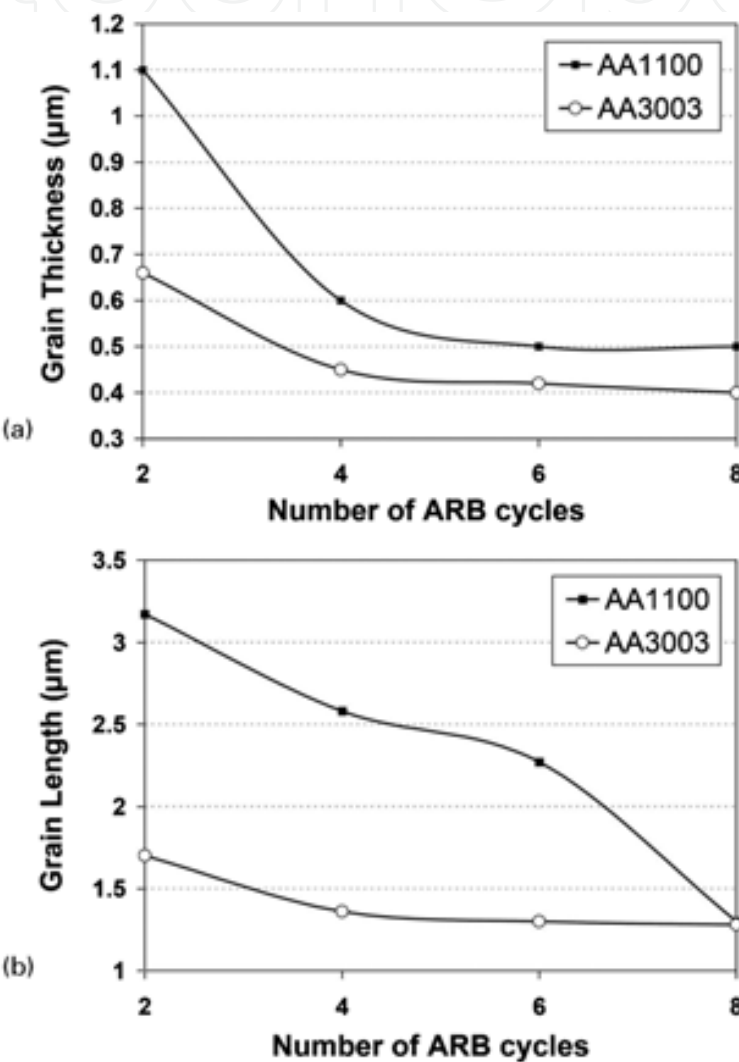
Fig. 6. Variation of microstructural parameters of aluminium sheets during ARB process, (a) grain thickness and (b) grain length

A general definition for the materials with a submicrometer grain structure proposed by (Prangnell et al., 2001) includes two main criteria: the average spacing of HAGBs must be less than 1 μm, and the fraction of HAGBs must be greater than 70%. The authors' observations proved that the development of such submicrometer or ultrafine grains in a single phase (AA1100) and a particle containing alloy (AA3003) occurs at different levels of strains during the ARB process. It was shown that (Heason & Prangnell, 2002a) the

evolution of ultrafine grains in the AA1100 alloy occurs by various mechanisms of grain refinement at different strains.
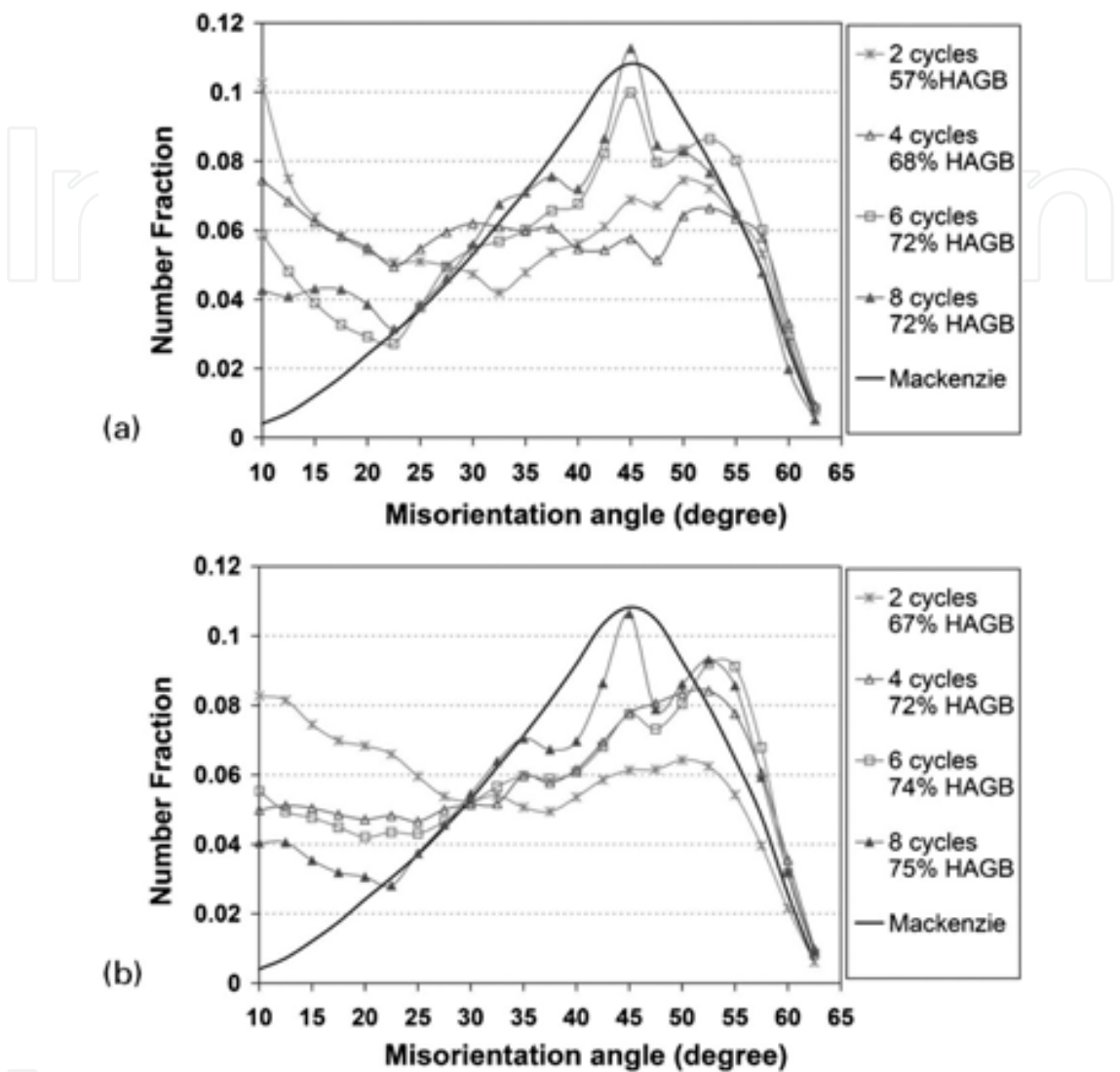

Fig. 7. Misorientation distributions in the samples of (a) AA100 and (b) AA3003 aluminium sheets processed by various ARB cycles

At low strains ($\varepsilon < 1.6$), grain subdivision is the dominant mechanism which leads to the formation of a fibrous microstructure of elongated grains. This mechanism also promotes the formation of subgrains surrounded by a high fraction of low angle grain boundaries (Fig. 4a) and some coarse unrefined bands which contain predominantly subgrains are seen in this specimen. At medium levels of strains ($1.6 < \varepsilon < 4.8$) the grain subdivision ratio decreases and the strain induced transformation of low angle to high angle grain boundaries caused by the accumulation of dislocations in exiting subgrain boundaries is the governing mechanism which results in a lamellar structure at the specimens processed by four and six ARB cycles (Figs. 4b and c).

The misorientation profiles plotted in Fig. 7 confirm the increase of HAGBs in expense of the LAGBs and the tendency of misorientation of the lamellar structure to a Mackenzie distribution. In comparison with the first sample, less pronounced unrefined regions of

subgrains are also seen in these samples. The proposed mechanism for grain refinement at high levels of strain (ε> 4.8) is the progressive fragmentation of thin lamellar grains into more equi-axed grain structures (Fig. 4d). The last mentioned mechanism enables the ARB process to develop a relatively homogeneous submicrometer grain structure in aluminium sheets.

Figure 5 displays that in comparison with the AA1100 alloy, in the AA3003 alloy which contains a significant volume fraction of second phase particles, an ultrafine grain structure develops at a much higher rate. It has been reported that two types of precipitates evolve in the AA3003 alloy: orthorhombic (Fe,Mn)Al$_6$ and cubic α-Al(Fe,Mn)Si (Rios & Padilha, 2003). The total volume fraction of these precipitates is between 4 and 5% and the large majority of them are elongated and have an average length between 1 and 5 mm. According to Fig. 7, the volume fraction of HAGBs after the second cycle in the AA3003 alloy is 67% compared with 57% in the AA1100 alloy. At the same time, the transverse spacing of HAGBs in these specimens is 0.66 and 1.1 mm respectively (Fig. 6a). This rapid refinement of grains in the AA3003 alloy at relatively low strains results from extensive generation of HAGBs in local deformation zones around the second phase particles. During deformation, large lattice rotation around the second phase particles leads to the increase of the local misorientation and production of new HAGBs. Dispersion of these particles also develops a random and more heterogeneous plastic flow behaviour within the matrix and promotes fragmentation of the lamellar structures seen in the AA1100 alloy. This behaviour as well as the gradual increase in the percentage of HAGBs and reduction in the grain aspect ratio during the next cycles results in the formation of a more homogenous submicrometre grain structure in the AA3003 alloy (Fig. 6). TEM micrograph depicted in Fig. 8 confirms that the grain size of the sample processed by 10 ARB cycles reaches a nanoscale value. The microstructure mostly consists of grains with a size in the range of 200-300 nm which are surrounded by clear boundaries.
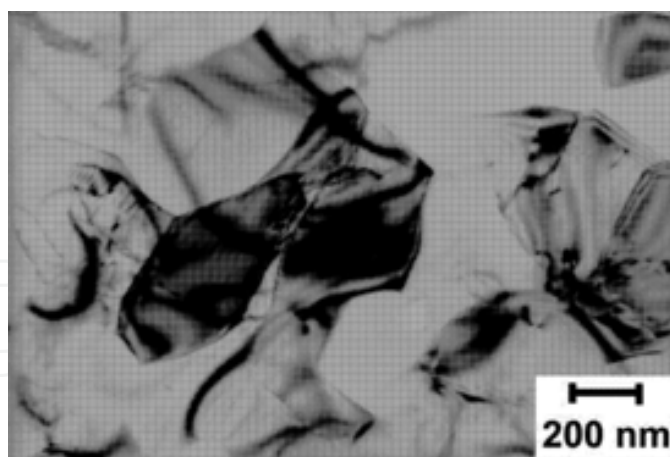

Fig. 8. TEM micrograph showing ultrafine grains in rolling plane of the AA1100 sample after 10 ARB cycles

3.1.2 ASB processing

Optical micrographs of the longitudinal sections of ASB samples are shown in Fig. 9. Previous study on the bond quality of spin-bonding process showed that the threshold thickness reduction for Al/Al bonding by conditions of this work is about 24% (Mohebbi & Akbarzadeh, 2010a). Therefore, it is expected that a good bond is obtained at thickness

reduction of 50%. While no interface was observed on the sections after polishing, the bond interfaces are distinguished by etching (Fig. 9). Since subsequent ASB cycles improve the previous bonds, the last bond interface of each specimen is clearer than the previous ones. It is obvious in this figure that the external layer undertakes more thickness reduction than the internal one at each cycle, so that the ratio of external layer thickness to internal one is between 0.40 and 0.45. It should be noted that during the process more elongation were observed in the length of external tube than the internal one, confirming the mentioned thickness strain distribution.

Number of ASB cycles	1	2	3	4
Fraction of the HAGBs	0.54	0.76	0.83	0.84
Grain thickness (nm)	409	306	176	186
Grain length (nm)	885	717	465	419

Table 3. Results of the EBSD analysis

TEM micrographs and the corresponding selected area diffraction (SAD) patterns of the specimens ASBed by one, two and four cycles are shown in Fig. 10. The specimen after one cycle shows a grain size of about 1.5 µm. Large number of subgrain boundaries can be observed in this specimen. The specimen after two cycles illustrates ultra-fine grains with the size of approximately 600 nm. The grain size of about 150 nm is observed in the 4-cycle specimen. The SAD pattern illustrates a more complex shape comparing to the first and second cycles of ASB.
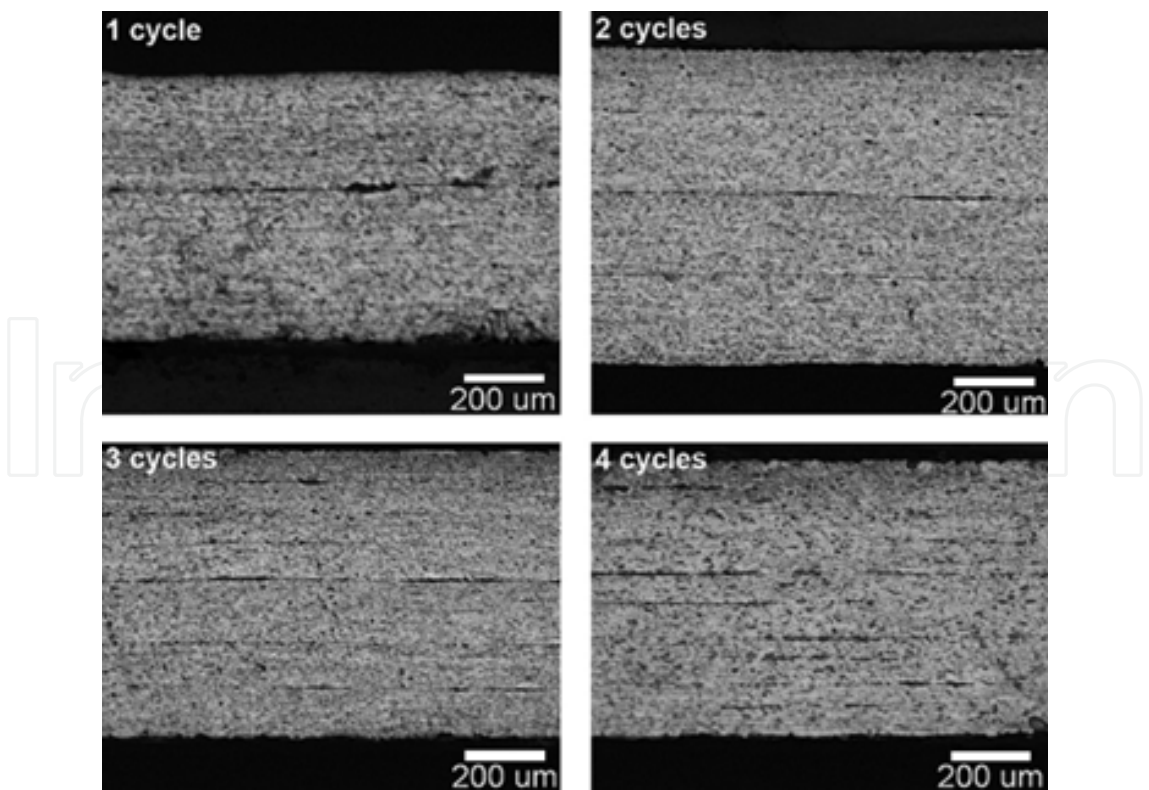

Fig. 9. Optical micrographs obtained from the longitudinal section of the AA1050 specimens after various cycles of ASB
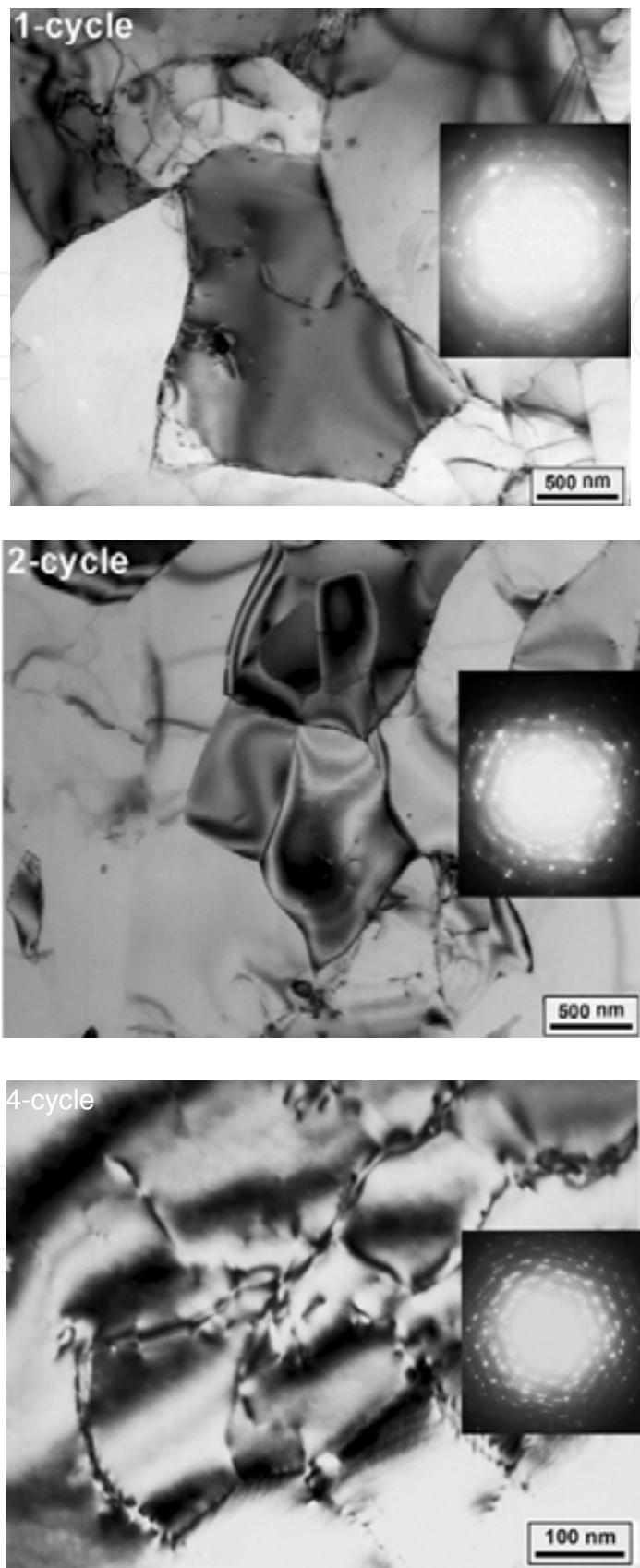
Fig. 10. TEM micrographs and SAD patterns of AA1050 specimens processed by one, two
and 4 cycles of ASB

Fig. 11 illustrates the low angle and high angle grain boundary maps recorded on the radial (r)-longitudinal (z) plane of the ASBed specimens. In this figure, which is obtained from the EBSD analysis, low angle grain boundaries (LAGBs) are depicted by red lines where the misorientation between two points of a step is between 2° and 15° and high angle grain boundaries (HAGBs) with misorientations larger than 15° are drawn in the black lines. Comparing to the very locally analysis of TEM micrographs, this figure clearly shows the
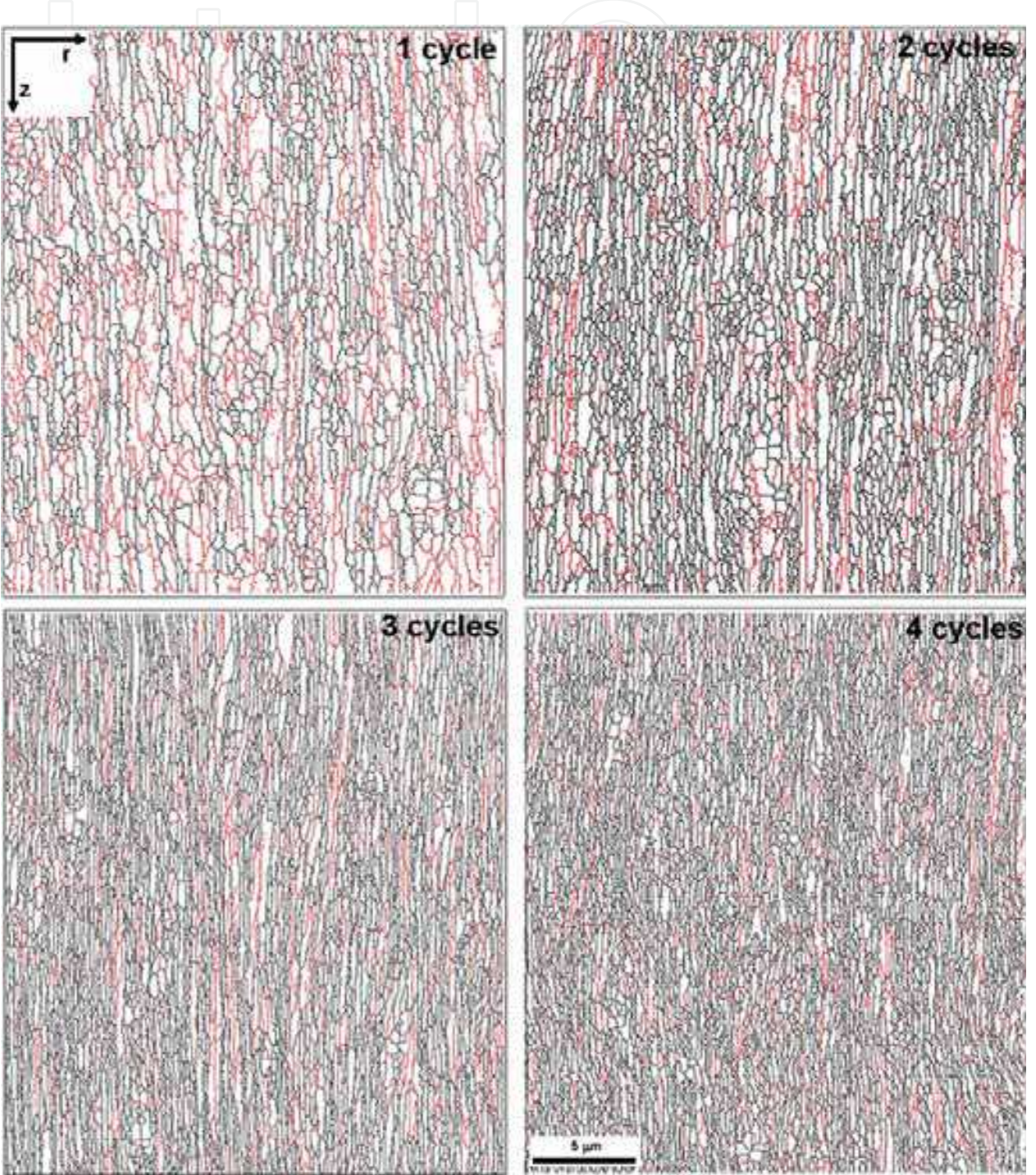
Fig. 11. High angle (black) and low angle (red) grain boundary maps of AA1050 specimens processed by various cycles of ASB

grain refinement and increment of HAGBs fraction by increasing the ASB cycles. Quantitative analysis of the EBSD patterns is presented in Table 3 and Figs. 12 and 13. Regarding the elongated grains, grain size is described by the grain thickness and grain length in radial and longitudinal directions, respectively. This is considered and applied for both subgrain and grain boundaries.

Fig. 12 demonstrates that both grain thicknesses and lengths decrease by increasing the ASB cycles, so that the grain thickness and length are, respectively, 186 and 419 nm after the fourth cycle. In addition to grain refinement, it can be seen in Figs. 11 and 12 that the HAGBs fraction is increased from 54% after the first cycle to 84% after the fourth cycle of ASB. The grain boundary misorientation increments through the ASB cycles are clearer in depiction of misorientation distributions, Fig. 13. The Mackenzie distribution for a random polycrystalline material is shown by black line. It is observed that while the misorientation distribution after the first cycle is considerably far from the random, it becomes much closer to a random distribution during the next ASB cycles.
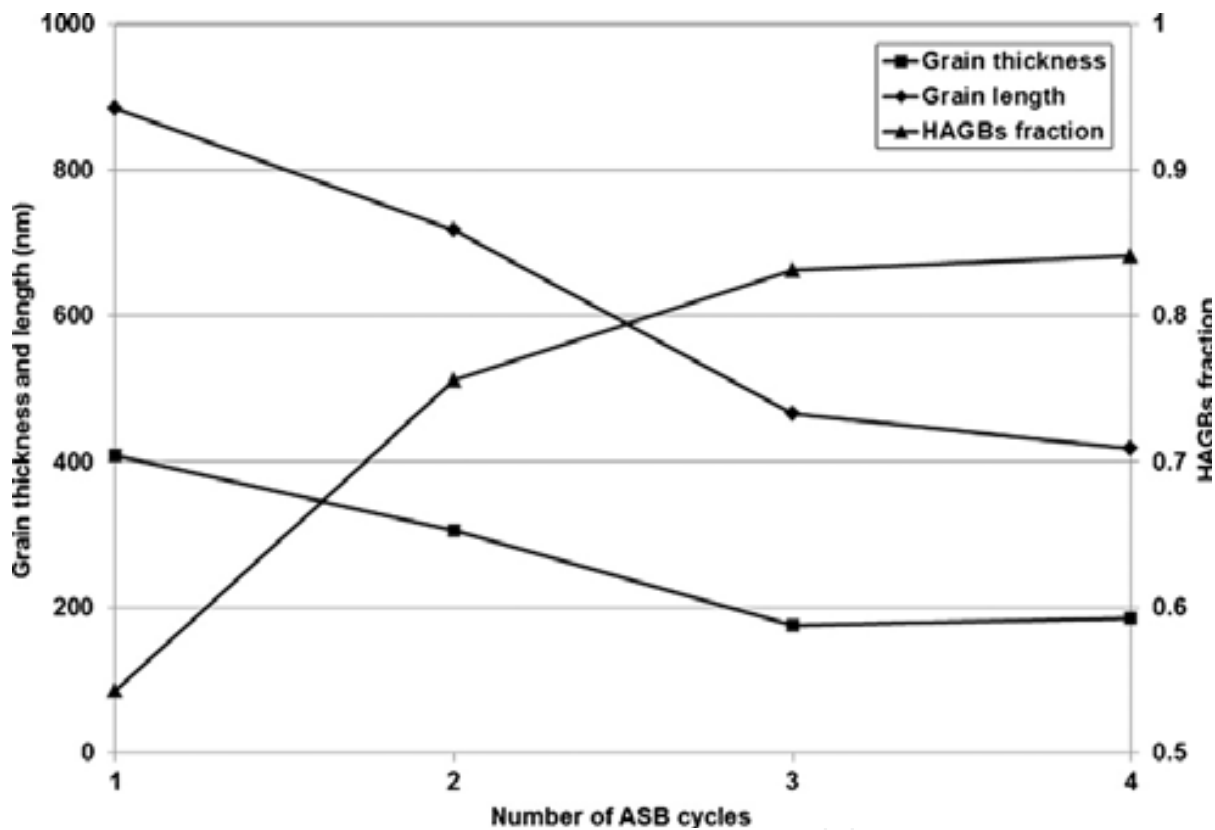

Fig. 12. Evolution of grain thickness and length and fraction of the HAGBs during the ASB cycles obtained from the EBSD analysis

An analytical model was recently developed (Mohebbi & Akbarzadeh, 2010a) to study the strain history of this process. In this model, the radial strain increment at each revolution is calculated. Total strain at each time is then determined by summation of these increments. The strain rate is calculated by dividing these strain increments to the deformation time of each one (Mohebbi & Akbarzadeh, 2010b). It was demonstrated that the material undergoes a small deformation with high strain rate at any exposure to roller, while at the time between the steps, the strain rate downfalls to zero. For thermally activated deformation

and restoration processes, which occur even at room temperature by large strains (Estrin et al., 1998), the microstructural evolution and flow stress are dependent on the deformation temperature, strain and strain rate. The strain rate ($\dot{\varepsilon}$) and deformation temperature (T) are included into the Zener–Hollomon Parameter (Z), which is defined as:

$$Z = \dot{\varepsilon} \, \exp (Q/RT) \tag{1}$$

where Q is the activation energy for operative process and R is the gas constant (Zener & Hollomon, 1944).
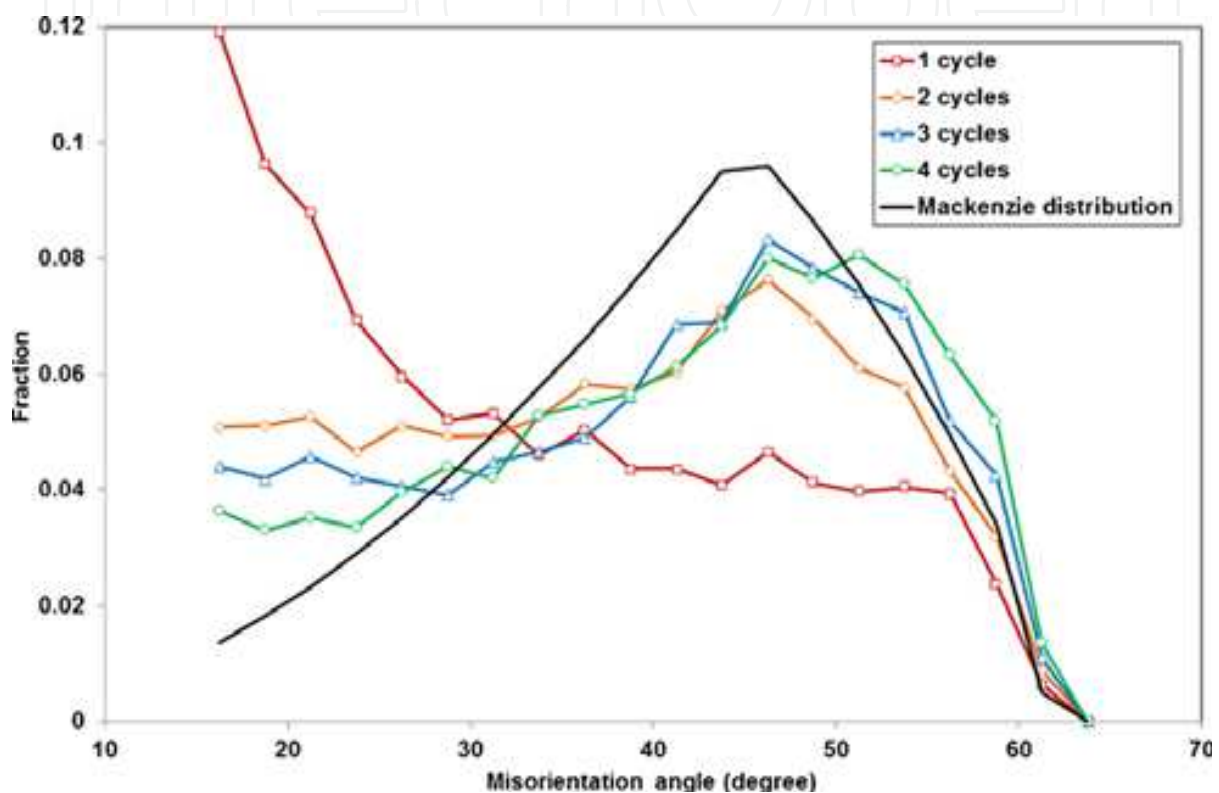
Fig. 13. Misorientation distribution of the specimens processed by various cycles of ASB comparing to the Mackenzie distribution

Generally, by increasing this parameter, subgrain size at dynamic recovery and steady state grain size at dynamic recrystallization are decreased and the flow stress is increased (Humphreys & Hatherly, 2004). Tsuji et al. (2003b) have studied the effect of strain rate on microstructural changes in deformation of the ultra-fine grained (UFG) aluminum produced by ARB. They had expected that higher speed of deformation can result in finer grain subdivision, because larger amount of dislocations would operate at higher strain rates. However, their results showed that grain size rather increases with increasing the strain rate, due to heat of deformation. Therefore, they concluded that higher strain rate and simultaneous cooling are favorable for producing finer grain size in SPD. However, as deformations with strain rates higher than 10 s⁻¹ are adiabatic processes (Ryazanov et al., 2003), simultaneous cooling is not effective on deformation temperature and therefore, conclusion of Tsuji et al. (2003b) cannot be correct.

Controlled cooling of the specimen in tensile test maintains the normal temperatures of the tests conducted at 10^{-2} to 10^{-1} s⁻¹. For higher strain rates, the only way is to perform the test

by applying strain in increments small enough to determine the negligible temperature rises during the incremental cooling periods (Sevillano et al., 1981). Therefore, it can be said that increasing the strain rate in common SPD processes causes a high temperature rise due to continuous induction of a large strain, which prevents significant promotion of Z. In case of ASB, however, it is possible to increase the strain rate without temperature rise. Deformation with high strain rate and low temperature rise is a very interesting characteristic of ASB process for evaluation of the pure effects of strain rate on the microstructural evolutions and resulted mechanical properties without temperature rise.

This research group's work has shown (Mohebbi & Akbarzadeh, 2010b) that due to large amount of redundant strain and high Zener–Hollomon parameter, as the characteristics of ASB process, the grain refinement and the rate of microstructural evolution are expected to be higher in comparison to other SPD processes. This grain refinement occurred by common mechanism of grain refinement in SPDs of pure aluminum. Increase of dislocation density and its accumulation in cell structure by dynamic recovery leads to formation of subgrains at early stages. This is followed by increase of the misorientations by strain induced transition of low angle to high angle grain boundaries at next stages (Pirgazi et al., 2008b). This mechanism is confirmed by the TEM micrographs and SAD patterns as well as the EBSD analysis. As can be seen in Figs. 11–13, a large fraction of LAGBs is formed after the first cycle. After the fourth cycle, while the grains are more refined, the fraction of HAGBs is considerably increased and the boundary misorientation distribution is close to the random one (Mackenzie distribution).

3.2 Microtexture

Figure 14 shows $\varphi_2 = 45$, 65 and 90° sections of the initial orientation distribution functions (ODFs) of both aluminium sheets before the ARB process (fully annealed sheets). It is seen that the initial texture of these samples is mainly composed of a dominant rotated cube {001}<100> which is characteristic of the recrystallisation state. The ODFs corresponding to the samples of Figs. 3 and 4 are illustrated in Figs. 15 and 16 respectively. Only the $\varphi_2 = 45$ and 90° sections of ODF are represented because these sections contain the most important texture components for ARB processed aluminium sheets. It is seen that the main texture components in the mid layers of both materials are Copper {1 1 2}<1 1 1> located at φ_1, Φ, φ_2 $\equiv$ 45, 65 and 90° and Dillamore {4 4 11}<11 11 8> at φ_1, Φ, φ_2 $\equiv$ 90, 27 and 45° sections and there is no evidence of shear components. The ODFs of these ARB processed samples were generally similar and the overall texture intensity and the concentration of the contour lines increase continuously with increasing strain. However, it should be noted that in comparison with the AA3003 alloy, a more severe texture was observed in AA1100 alloy during the ARB process and the strength of the overall textures developed at the eighth cycle was 18.4 and 28.2 times the random levels, respectively.

The presence of second phase particles can also change the microtextural evolution in the ARB processed aluminium sheets. The comparison of the ODFs presented in Figs. 15 and 16 indicates that the developed texture in the AA1100 alloy is much stronger than the particle containing alloy. The evolution of a strong texture during the ARB process is attributed to the cyclic nature of this process. Heason and Prangnell (2002a) investigated the texture evolution during the ARB process of the AA1100 aluminium sheets by using a model based on the FC-Taylor approach. According to their model, the surface shear texture which deforms in plane strain compression (in the mid layer) rotates towards the copper orientation during the next cycle. In contrast, this model predicts that all the rolling
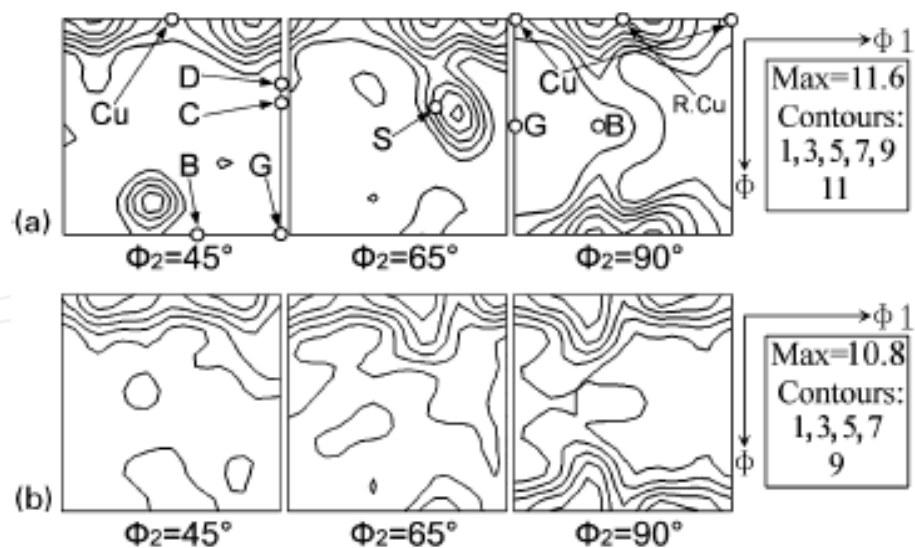
Fig. 14. φ_2=45, 65 and 90° sections of ODF of fully annealed (a) AA3003 and (b) AA1100 aluminium sheets before ARB process: standard texture components are indicated with symbols: Cu: cube; R.Cu: rotated cube; C: copper; B: brass; G: Goss; D: Dillamore
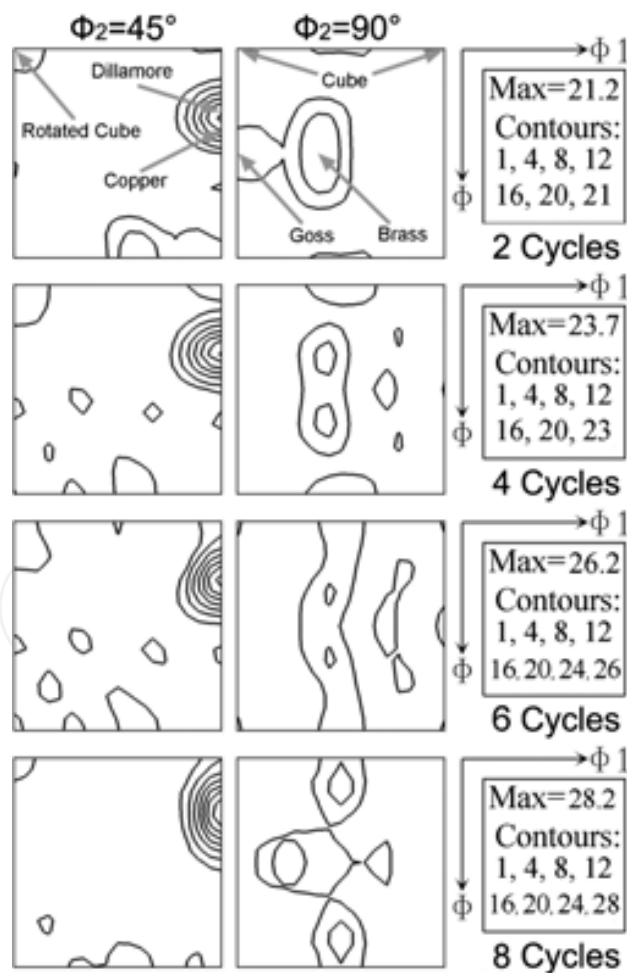

Fig. 15. φ_2=45 and 90° sections of ODFs corresponding to AA1100 samples processed by various ARB cycles: these ODFs were calculated assuming orthorhombic sample symmetry

components (copper, S and brass) rotate towards the shear orientation when they come to the surface of the sheet. This can also explain the increase in the intensity of copper and Dillamore components (which are close to each other) as the main texture components observed in this study. These authors have also reported that this strong texture leads to the development of coarse unrefined bands and prevents the full grain refinement to a submicrometre scale during the ARB process of a single phase aluminium alloy. Whereas, the presence of the second phase particles in the AA3003 alloy results in large local lattice rotation and can cause different textures compared with the rest of the matrix. Thus, the overall texture intensity will be much weaker than the AA1100 alloy.
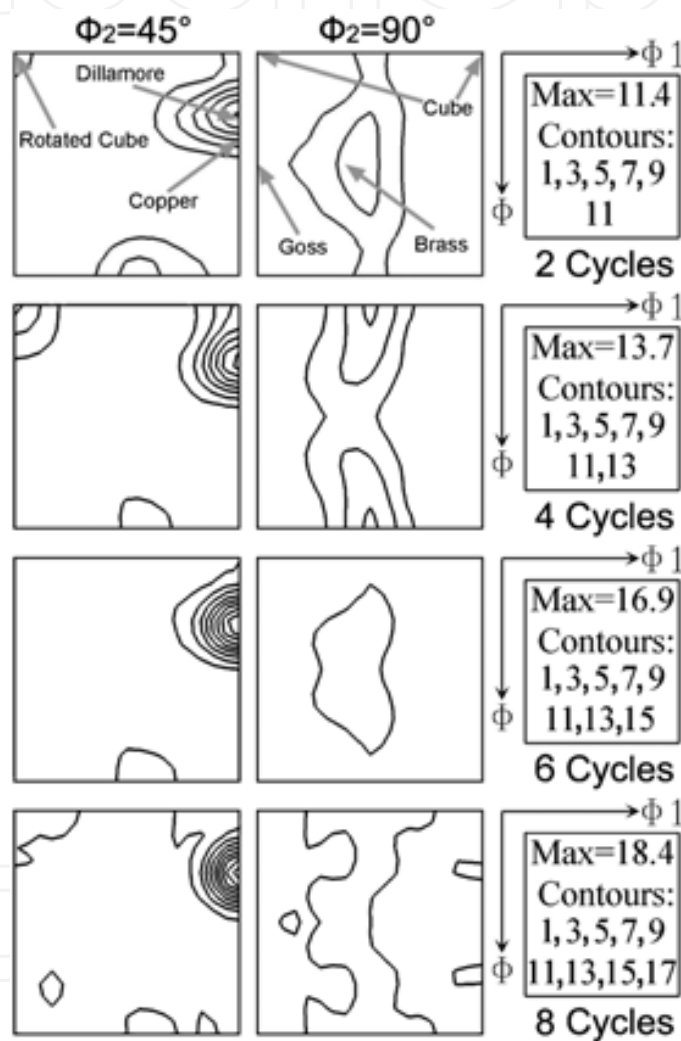
Fig. 16. φ_2=45 and 90° sections of ODFs corresponding to AA3003 samples processed by various ARB cycles

Kim et al. (2005) reported similar results in ARB processed AA8011 aluminium alloy. According to their study, the textural change from a shear texture to a rolling texture at the sheet centre during the ARB process contributed to an increase in the fraction of high angle boundaries. Also, a large number of second phase particles in the AA8011 alloy sheets weakened the texture intensity which is due to the inhomogeneous deformation around the second phase particles. A weak and more spread texture caused by the presence of the

second phase particles contributes to the transformation from low angle subgrain boundaries to high angle grain boundaries by increasing the misorientation between two adjacent subgrains and removes the unrefined bands from the microstructure. For a better understanding of the texture evolution, the main FCC fibers were calculated and plotted in Fig. 17. Generally, with increasing the number of cycles, the intensity of the α fiber decreased while the intensities of the β and τ fibers increased. The α fiber, running from Goss to brass in Fig. 17a, indicates how the brass component decreased during the ARB process. It is seen that during all ARB cycles the intensity of Goss component is negligible. Fig. 17b shows the intensity of the β fibers.
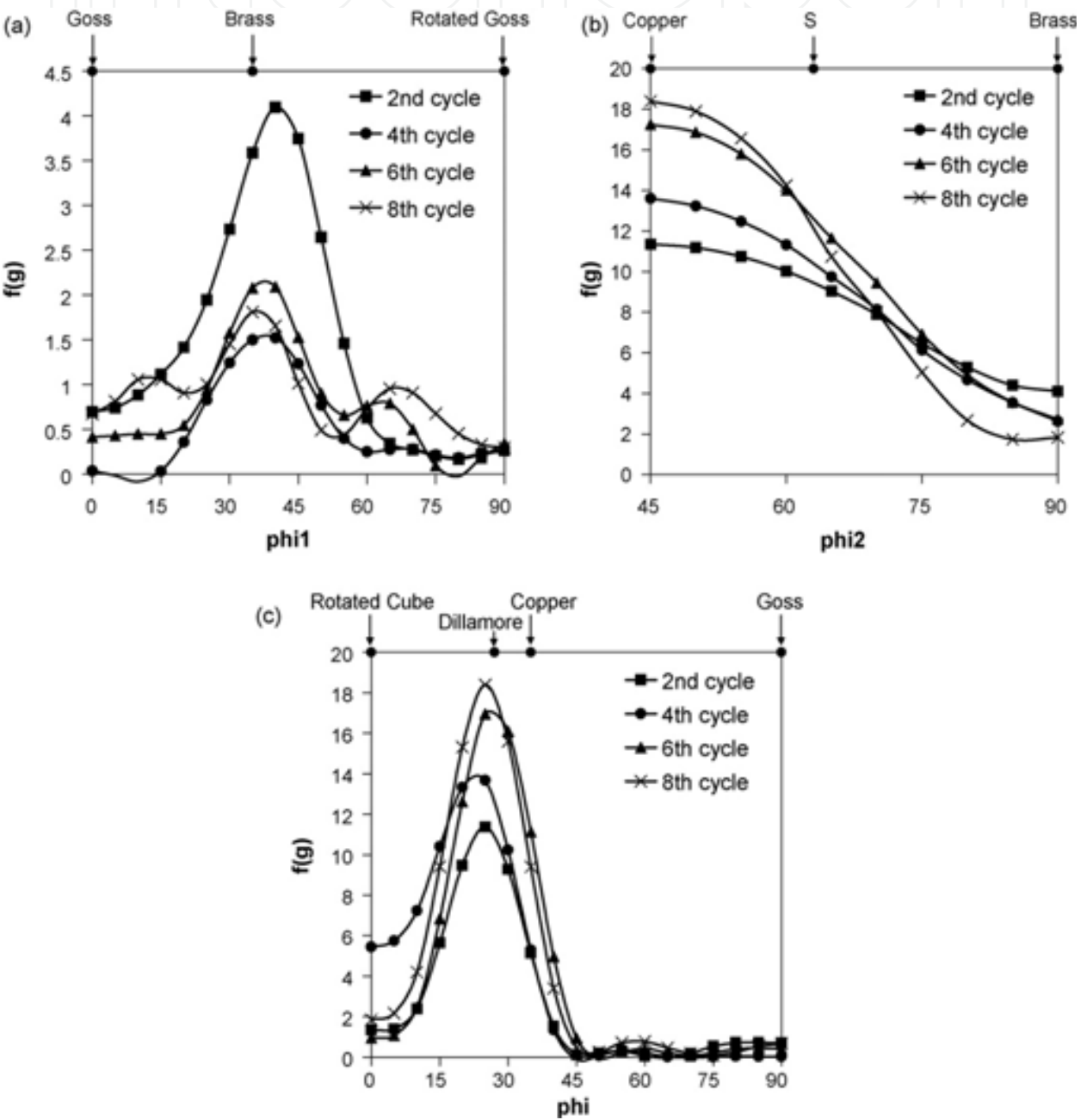
Fig. 17. Intensity of the FCC fibers in the ARB processed aluminum sheets: (a) β-fiber, (b) τ-fiber, and (c) α-fiber

It shows that in the early stages of the ARB process the intensity of the β fiber, running from copper over S to the brass orientation, is almost homogeneous, but with increasing the number of cycles the intensity of the copper component gradually grows at the expense of the brass and S components. The τ fiber is presented in Fig. 17c. It is observed that in this material the texture evolution is mainly centered around the copper and Dillamore components, and with an increasing number of cycles these components further intensify.

3.2.1 Modeling of texture evolution

In order to interpret the texture change involved in the ARB process, the texture development was simulated with the Alamel model (Van Houtte et al., 2005, 2006). The deformation during ARB processing is approximated by a two-dimensional velocity gradient tensor which is composed of a compressive strain (ε_{zz}, $\varepsilon_{yy} = 0$ and $\varepsilon_{zz} = -\varepsilon_{xx}$) added with a simple shear strain (ε_{xz}). The texture simulations have been performed on the initial texture of Fig. 14 for different strain modes with various ratios of the simple shear component (ε_{xz}) to the plane strain compression components. The imposed shear during the ARB process is characterized by the shear coefficient K ($K = \varepsilon_{xz}/\varepsilon_{zz}$).

The texture simulation for the subsurface region has been performed with a large value of the shear coefficient (K= 2.4) due to localization of shear deformation in this region. The texture prediction for the mid-thickness part has been performed under the deformation condition with K= 0.1. It is assumed here that even in the middle layers of the sheet there will still be a small amount of frictional shear as the ARB experiment was carried out in totally dry conditions (i.e. without lubrication). Due to the specific stack-and-roll geometry of the ARB process, the subsurface texture after the first ARB pass appears in the central layer of the composite sample in the second ARB pass. Hence, in order to simulate the texture evolution in the middle layer in the ARB pass n_i the Alamel model was applied on the subsurface from previous pass $n_{(i-1)}$ with a deformation mode that was characterized by K= 0.1. Fig. 18 presents results of the texture predictions for second, fourth, sixth and eighth ARB cycles. The calculated textures are in very good qualitative and quantitative agreement with the experimentally measured ODFs (Figs. 16 and 18).

The model calculation has produced the textures which exhibit a strong rolling β-fiber. It is important to notice, though, that the Dillamore and S components are far more important than the brass orientation, which corresponds very well to the experimentally observed texture, cf. Fig. 16. Furthermore, intensities of both S and brass orientations increase insignificantly whereas a considerable strengthening of the Dillamore orientation is observed during ARB process. Hence, it is shown here, on the basis of crystal plasticity modeling, that the sequence of rolling, cutting and stacking, which is characteristic for the ARB process eventually triggers a mechanism which leads to strengthening of the Dillamore component in the middle layers of the ARB sample.

Rotation of different texture components during ARB cycles, i.e. shear to copper and Dillamore components in the midsection under the plane strain compression mode and copper, S and brass to the shear component in the surface layer due to the shear deformation, is the unique feature of ARBed aluminum sheets (Heason & Prangnell, 2002a; Kim et al., 2005). This can be considered as the result of introduction of surface layer to the midsection during the next cycle and it is also associated with the increase in the number of interfaces. In fact, these interfaces induce additional strain during rolling and are responsible for the unique property.
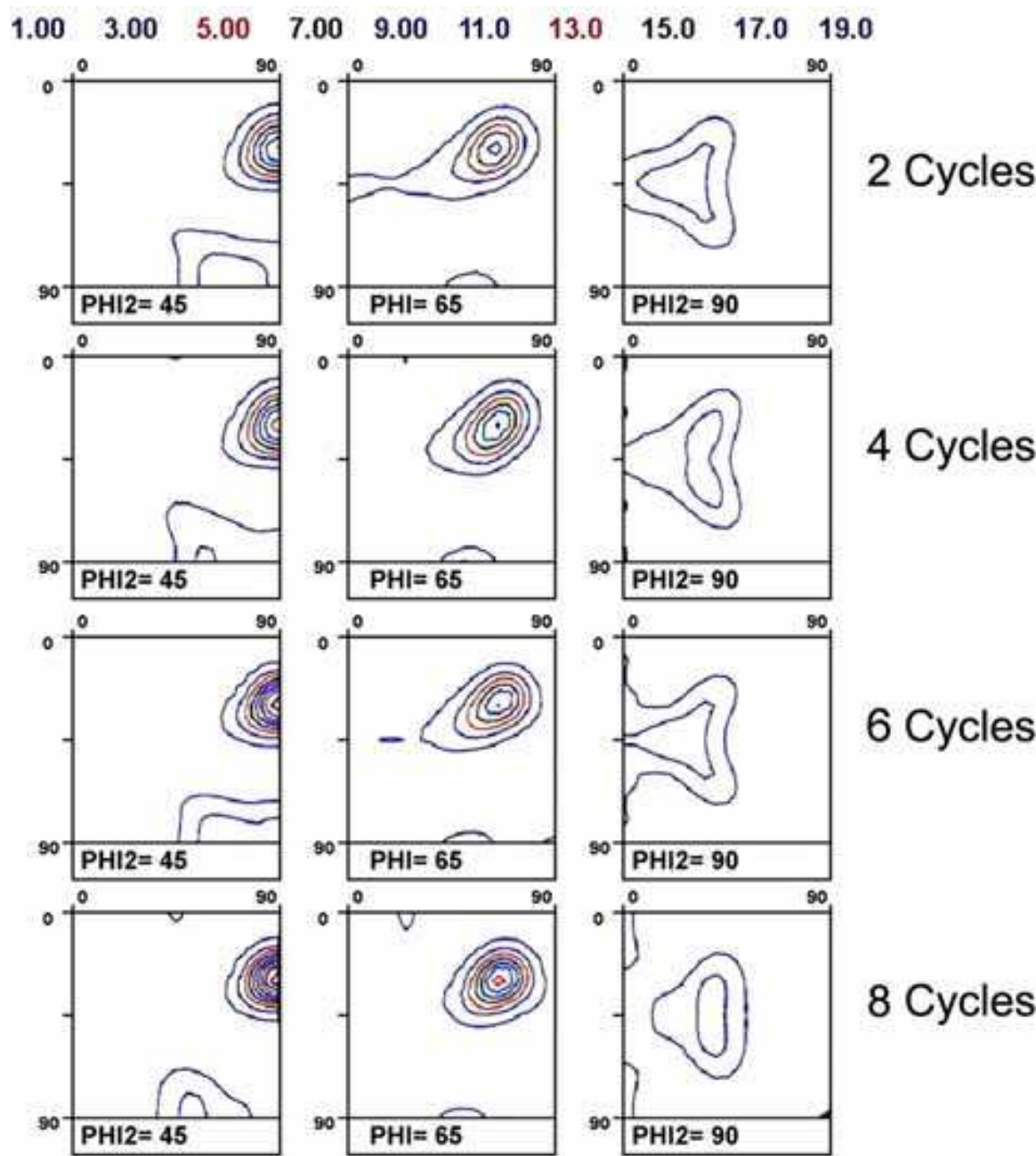
Fig. 18. Simulation of the texture development in the center region during different ARB cycles

3.3 Mechanical properties
3.3.1 ARB samples

Second phase particles in AA3003 alloy can also accelerate the rate of dynamic recovery which is very likely to occur in warm rolled aluminum sheets. Accumulation of dislocations in the vicinity of these particles leads to rapid transformation of low angle sub-grain boundaries to high angle grain boundaries and decreases the dislocation density inside the grains. Static recovery during pre-heating may also contribute to the reduction of dislocation density and promote the softening behavior. The variation of the microhardness with increasing strain during the ARB process confirms the occurrence of recovery in this

phenomenon, Fig. 19. The hardness curve in this figure corresponds well with the microstructural changes mentioned above. Initial work hardening caused by the reduction of grain size and the growth of dislocation density inside the crystalline lattice leads to a rapid increase in microhardness at the first ARB cycle (ε_{vM} = 0.8). During the following cycles, static or dynamic recovery caused by the interpass annealing treatment, the heat of deformation and the accumulation of dislocations in the vicinity of the second phase particles, prevents a further increase of the hardness and a plateau around 80 HV is established.

An interesting feature of this figure is the significant increase of the hardness value (close to two times of the initial value) after the eighth cycle, while the sample exhibits a fully recovered microstructure and probably still provides an acceptable ductility. According to the results presented here, different mechanisms of grain refinement can be attributed to the different levels of strain. During the first two cycles of ARB (ε < 1.6) grain subdivision is the dominant mechanism. This mechanism promotes the formation of a fibrous microstructure of elongated grains.
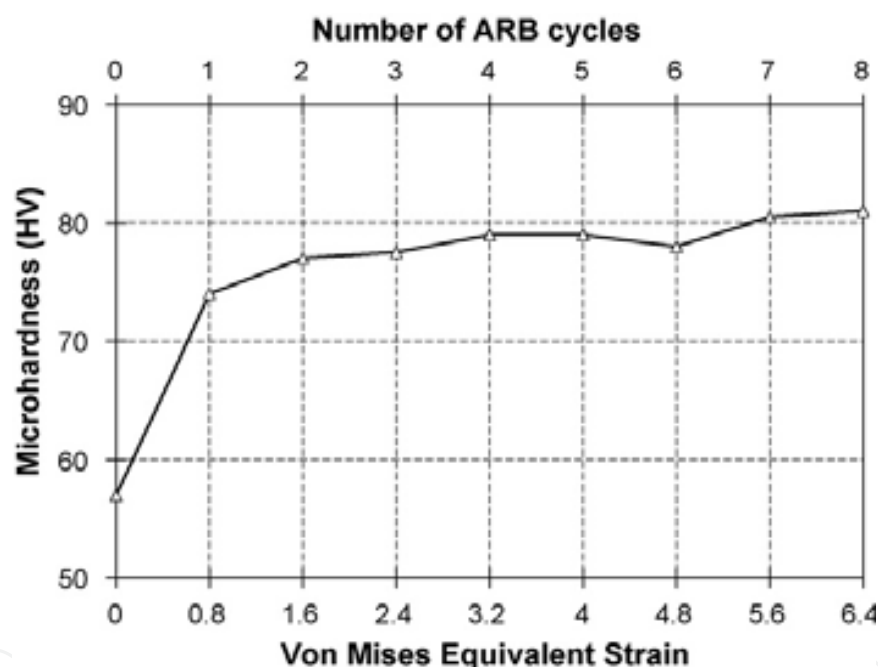

Fig. 19. Variation of Vickers microhardness of AA3003 alloy with increasing strain during ARB process

The results of the mechanical properties clarified that the strength of the ARBed aluminum sheets increases with increasing the number of cycles, Fig. 20. In order to study the relation between the mechanical properties and the microstructural changes, the tensile strength and the 0.2% yield strength were plotted as a function of minus square root of grain size in Fig. 21. The strength of the ARBed aluminum sheets is in a good conformity with Hall–Petch relationship, even for submicron grain structures. It was shown (Pirgazi et al., 2008b) shows that the amount of work hardening after yielding is rather small and necking occurs suddenly and causes the limited uniform elongation. It should be noted that the described microstructural evolution corresponds to the changes in mechanical properties very well. This suggests that the strength of the ARB samples is mainly attributed to grain boundary

strengthening, though the details of the strengthening mechanism in the SPD materials should be discussed more. As has been already known, the ARB processed specimens have the dislocation substructures inside the UFGs as well as the elongated grain morphology. This means that the strength of these specimens might be affected not only by grain refinement strengthening but also by strain hardening. It has been proposed that when a deformation structure consists of a mixture of low and high angle grain boundaries, the strength can be considered as the sum of dislocation strengthening from LAGBs and grain size strengthening from HAGBs (Hansen, 2004). However, the detailed discussion about the Hall–Petch relationship and strengthening mechanisms should be done in the future works. In a similar study by Park et al. (2001) on AA6061 alloy processed by the ARB at 250 °C it has been reported that the rapid increase in strength at relatively low strains is mainly due to the work hardening caused by an increase in dislocation density and formation of the sub-grains.
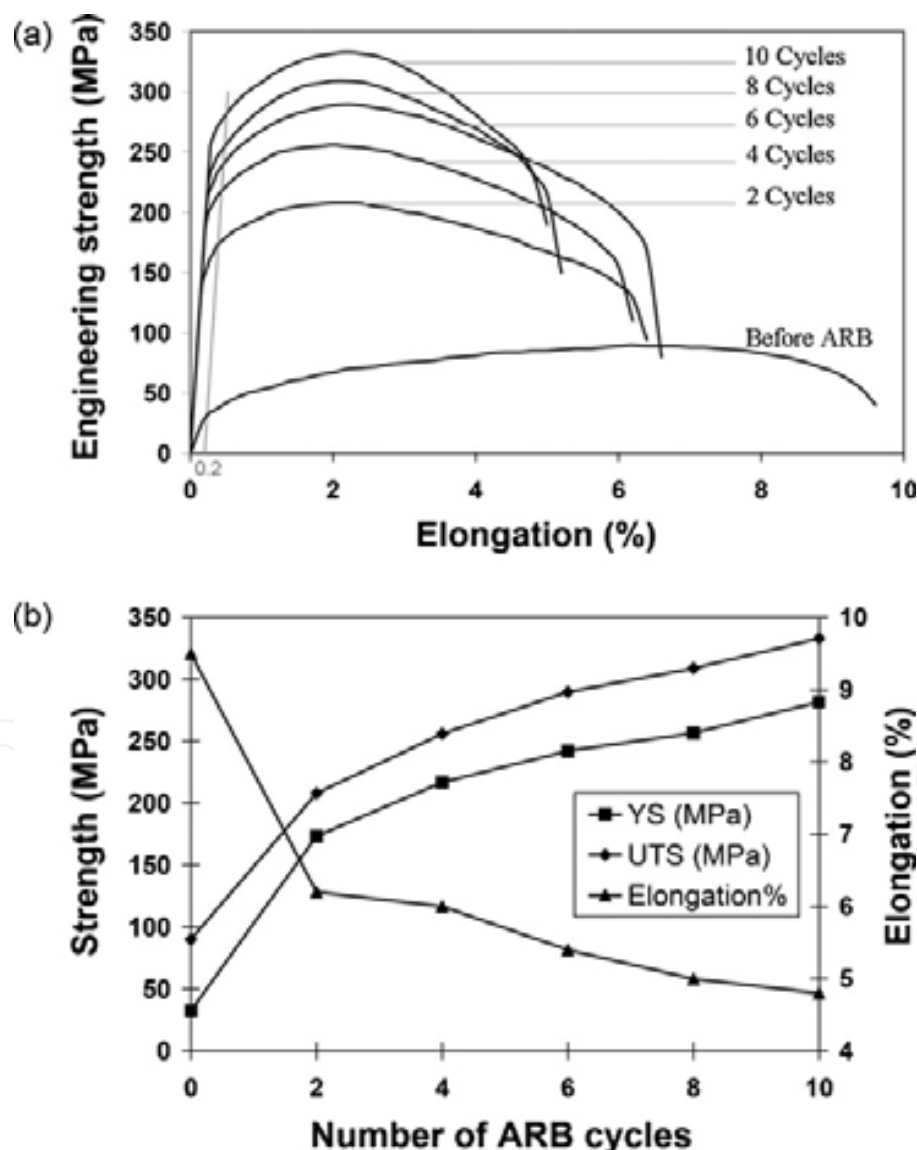

Fig. 20. (a) Engineering stress–strain curves and (b) the corresponding tensile properties of AA1100 aluminum sheets processed at different ARB cycles

During the following cycles, in which the incremental increase of the strength becomes smaller, the dislocation density is almost constant (Parh et al., 2001; Costa et al., 2005). The low density of dislocations at relatively high strains is due to the dynamic recovery (Costa et al., 2005), or absorption of dislocations into the grain boundaries (Prangnell et al., 2001). In any way, the increase of the volume fraction of ultra-fine elongated grains due to increase in the fraction of HAGBs can be contributed to the strengthening in the medium levels of strain ($1.6 < \varepsilon < 4.8$). Finally, the large strength at relatively high strains ($\varepsilon > 4.8$) can be explained by the development of ultra-fine grained structures.
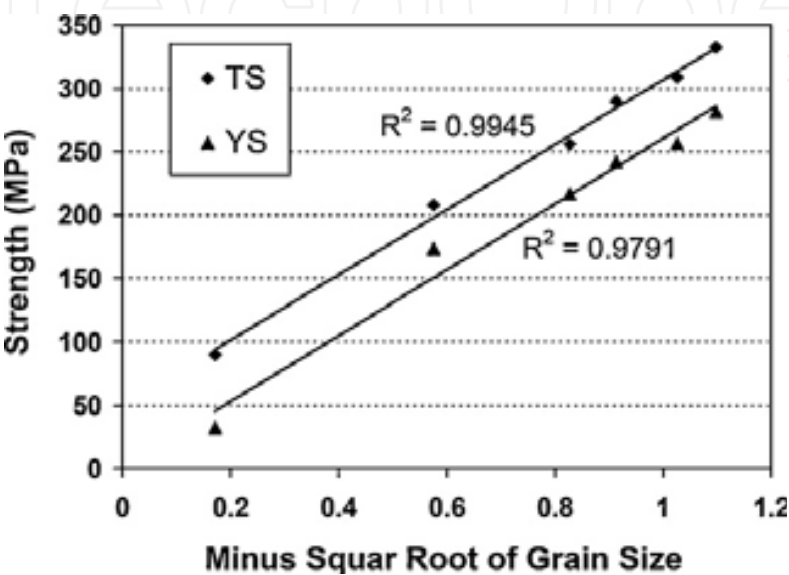
Fig. 21. Strength of ARBed AA1100 aluminum sheets versus the grain size. The grain sizes reported in this figure are the size of grains bounded by high angle grain boundaries
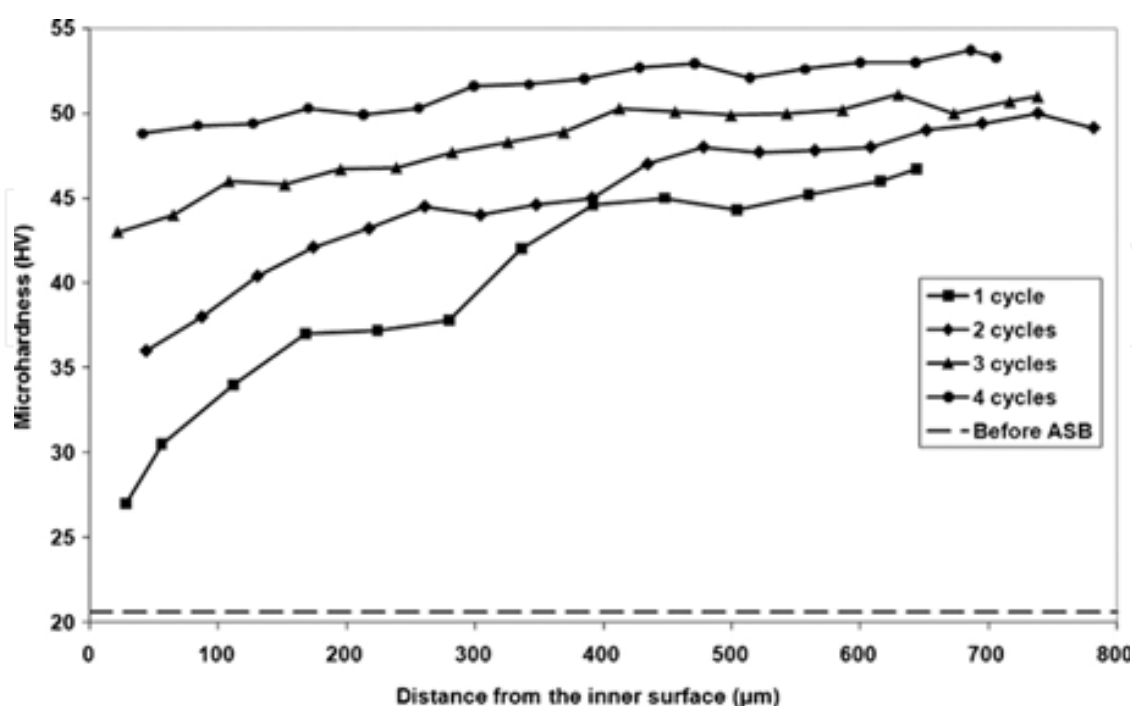

Fig. 22. Distribution of microhardness across the thickness of ASBed specimens

3.3.2 ASB samples

Distributions of microhardness across the thickness of specimens are compared in Fig. 22. The hardness of annealed specimen before ASB is shown by a dash line. It can be seen in this figure that the hardness is increased from the inner layers to the outer ones. Two trends in the hardness evolutions during the ASB cycles can be derived from this figure. First, the degree of hardness is increased, and second, the hardness distribution across the thickness of the tubes is homogenized. Fig. 23 shows the tensile stress–strain curves of the ASBed tubes.

Tensile properties derived from these curves are summarized in Fig. 24. The yield strength (at 0.2% offset strain) and the tensile strength are increased by the ASB cycles, although the growth rate is diminished. So that, the yield strength is increased up to 194 MPa after four cycles of ASB, which is about five times higher comparing to the initial material (40 MPa). Fig. 24 also shows that the difference between the yield and the tensile strengths is slightly decreased during the ASB cycles. Regarding the rupture elongation, a sharp drop is observed after the first cycle from 38% to 9%. Decrease of the elongation at subsequent cycles is quite low as compared to that of the first cycle. Hardness distribution across the thickness of the tubes confirms that materials below the outer surface undergo heavier plastic strain in comparison to the internal ones. This is due to not only higher thickness reduction but also higher redundant strains at the outer regions (Mohebbi & Akbarzadeh, 2010c).

Although this inhomogeneous hardness distribution is observed at all specimens, its intensity is decreased by increasing the number of ASB cycles. Two reasons can be mentioned for this scheme of hardness evolution. First, at each cycle of ASB, a tube is used as internal tube and so, its severely strained external layer is located within the interior regions. By this periodical entrance of the highly deformed outer materials within the thickness, the hardness distribution becomes more homogeneous by increasing the number of ASB cycles. Second, due to saturation of dislocation density and microstructural evolutions, the hardness and strength are always saturated at large strains (Valiev et al., 2000). Therefore, despite of inhomogeneous deformation, hardness becomes homogenized at large strains.

As it can be seen in Figs. 23 and 24, the yield strength and the tensile strength of the specimens are increased by increasing the ASB cycles, although its rate is gradually diminished. Grain refinement by mentioned mechanism, i.e. increase of dislocation density and formation of subgrains at early stages as well as increase of the misorientations at next stages are responsible for this strengthening (Pirgazi et al., 2008b; Sevillano et al., 1981). While based on this mechanism a steady state plateau is expected for strength of material, Fig. 24 shows that yield and tensile strengths are continuously increased. One may conclude that the strain induced by four cycles is not enough for strength saturation, especially at high value of Z in this work. However, it is shown that this continuous increase of the strength can be attributed to the through thickness inhomogeneity of hardness. Considering the mentioned hardness evolutions, it can be said that outer materials are severely work hardened after the two first cycles in comparison to inner ones. Therefore, in spite of strength saturation of the outer material, inner material has the possibility of work hardening at following cycles. This work hardening has two effects on the tensile properties. The first effect is continuous increase of the strength. By increasing the ASB cycles, inner materials are work hardened and therefore, the strength is increased. The second effect is related to the ratio of tensile to yield strength in tensile tests. As a result of work hardening

of the inner materials, the overall flow strength of the specimen is increased during tension. That is why there is a high difference between the yield strength and the tensile strength in this work in comparison to that of ARB (Pirgazi et al., 2008b). By this explanation, more hardness inhomogeneity causes higher ratio of tensile to yield strength. Therefore, decrease of the difference between the yield and tensile strengths by the ASB cycles in Fig. 24, is mostly related to the hardness homogenization.
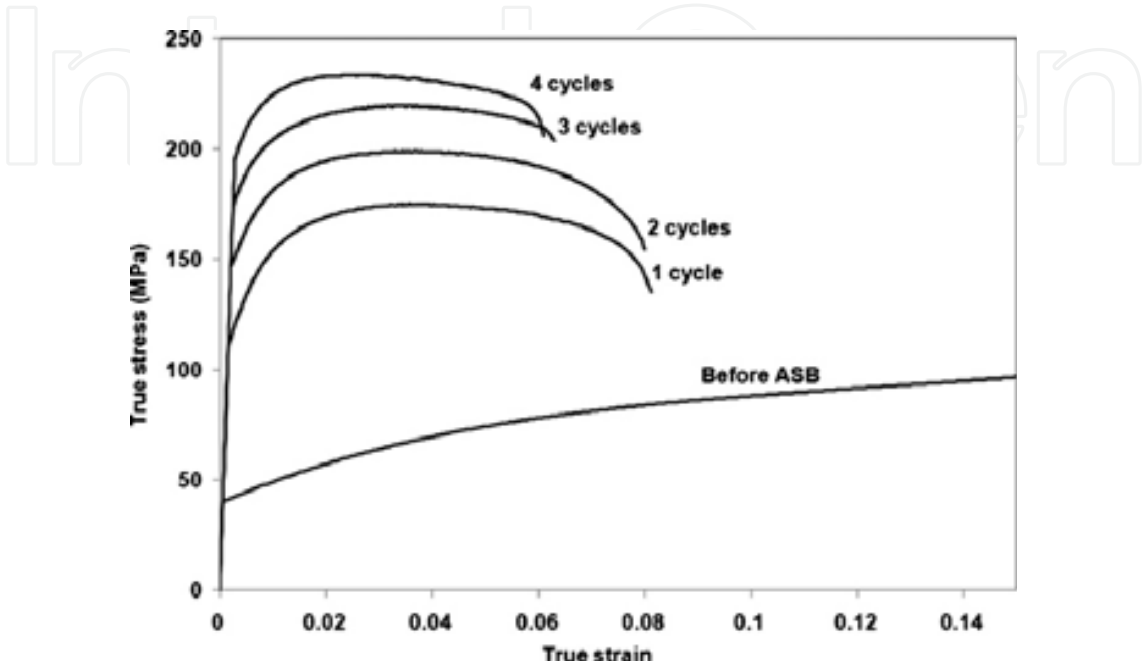
Fig. 23. Tensile stress–strain curves of the tubes processed by various ASB cycles
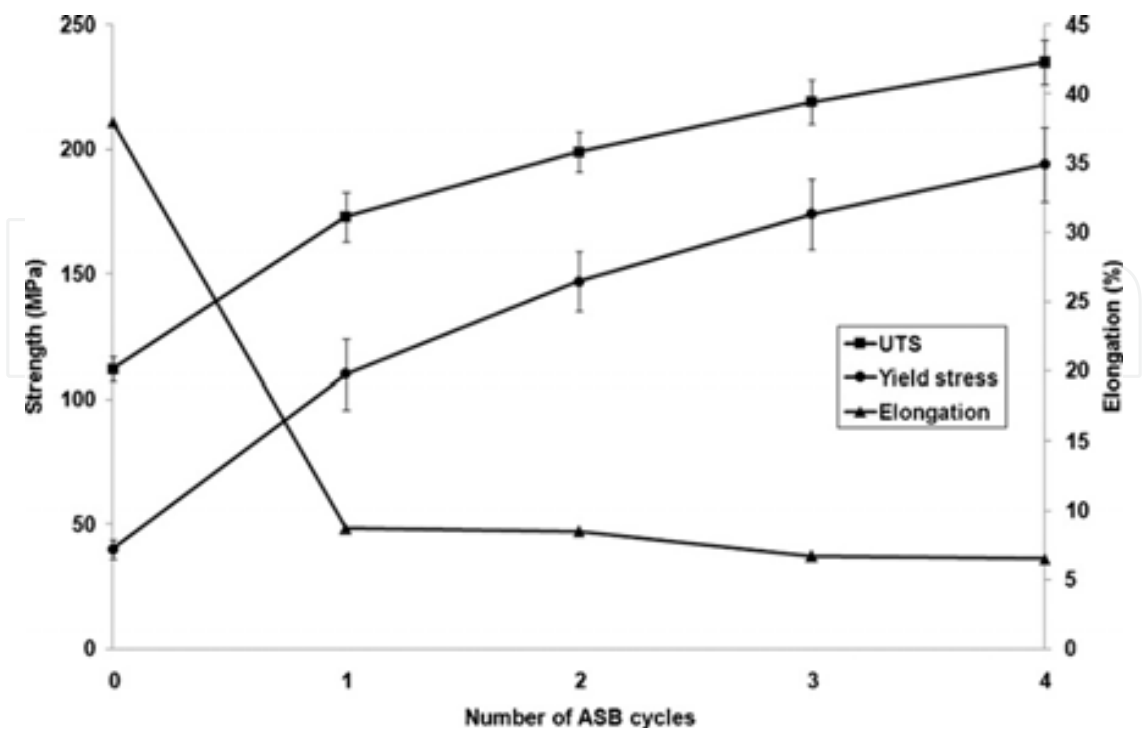
Fig. 24. Development of the tensile properties of tubes processed by various ASB cycles

Fig. 24 demonstrates a severe drop in elongation after the first cycle of ASB while its rate of reduction is very low at next cycles. This result is similar to the reported ones for ARB (Lee et al., 2002; Pirgazi et al., 2008b). Uniform elongation, which is reduced by increasing the ASB cycles, is related to onset of the plastic instability or necking. Plastic instability, on the other hand, is a function of work hardening and consequently, of the ratio of tensile to yield strength (Semiatin & Jonas, 1984). Therefore, it can be said that since this ratio is decreased by increasing the ASB cycles, the uniform elongation is decreased. In other words, inner materials of specimens after the early cycles of ASB, whose work hardening is not saturated, are work hardened during the tensile test, leading to delay in necking. At next cycles, due to saturation of work hardening across the entire thickness, plastic instability starts earlier and causes a less uniform elongation.

It is seen in Fig. 23 that post-uniform elongation includes a considerable portion of the total elongation. Previous studies on SPD have demonstrated that strain rate sensitivity of fcc metals increases by decreasing the grain size (Wang & Ma, 2004; Wei et al., 2004). High strain rate sensitivity, on the other hand, causes the increase of both uniform and post uniform elongations (Semiatin & Jonas, 1984). Takata et al. (2008) have illustrated that uniform elongation of commercially pure aluminum increases with increasing the strain rate in the specimens with a grain size larger than 1 μm, while post-uniform elongation increases with increasing the strain rate in the sub-micrometer grain size specimens. Therefore, it can be concluded that high strain rate sensitivity is effective on post-uniform elongation of aluminum with sub-micron grains. In fact, the high magnitude of post-uniform elongation in Fig. 23 can be mostly related to the high strain rate sensitivity.

4. Conclusions

EBSD analysis confirmed that the development of UFGs by ARB process is carried out via several mechanisms at different levels of strain. Grain subdivision as well as development of sub-grains is the major mechanism at the early stages of ARB. Strain induced transition of low angle to high angle grain boundaries and the formation of a thin lamellar structure occurs at the medium levels of strain. Finally, the progressive fragmentation of these thin lamellar structures into more equi-axed grains is the dominant mechanism at relatively high strains which leads to reduction of grain size to less than 500 nm. The presence of second phase particles in AA3003 aluminum sheets promotes the grain refinements and accelerates the occurrence of dynamic recovery. With an increasing number of cycles, the overall texture intensity increases and a very strong texture is developed which exhibits a limited number of sharp components. Large lattice rotation around these particles leads to the increase of local misorientation, evolution of a much weaker texture and development of a more homogeneous submicrometre grain structure in the AA3003 alloy. The Dillamore and the copper components are the main texture components of this material and they are sharpened with increasing the number of cycles. This texture evolution could be modeled with the Alamel crystal plasticity model and taking into account the specific geometry of the ARB process.

Generally, with increasing the number of cycles, the intensity of the α fiber decreased while the intensities of the β and τ fibers increased. It is shown that in the early stages of the ARB process the intensity of the β fiber, running from copper over S to the brass orientation, is

almost homogeneous, but with increasing the number of cycles the intensity of the copper component gradually grows at the expense of the brass and S components.

It is demonstrated that due to incremental deformation in ASB process, high value of strain rate without considerable temperature rise is applied, leading to a high degree of Zener–Hollomon parameter, as a characteristic of this SPD process. The grain structure of commercially pure aluminum is refined by this process and an average grain thickness and length of 186 and 419 nm are developed after the four cycles of ASB, respectively. TEM micrographs and SAD patterns as well as the EBSD analysis indicate that this grain refinement occurred by formation of subgrains at early stages of severe deformation followed by increase of the misorientations by transition of low angle to high angle grain boundaries at the next stages.

The characterization of mechanical properties revealed that the strength of the aluminum sheets considerably increased by the first two ARB cycles which is attributed to work hardening caused by increase in dislocation density and formation of subgrains. It was also included that the strength of ARBed aluminum sheets obeys the Hall–Petch relationship and corresponds well with microstructural variations. Microhardness distributions across the thickness of the tubes illustrate that because of high equivalent strain at outer regions, the hardness is increased from the inner regions to the outer ones. Due to periodical entrance of the external layer within the thickness and the consequent hardness saturation, the hardness and its homogeneity is increased with increase of the ASB cycles. The yield and tensile strengths of the material are significantly increased up to the values of 194 and 235 MPa, respectively. The scheme of hardness development leads to decrease of the ratio of tensile strength to yield strength and consequently to decrease of the uniform elongation.

5. Acknowledgments

6. References

Berski, S., Dyja, H., Maranda, A., Nowaczewski, J. & Banaszek, G. (2006). *Journal of Materials Processing Technology*, Vol. 177, pp. 582–586

Chen, Z., Ikeda, K., Murakami, T, Takeda, T., Xie, J.X. (2003). *Journal of Materials Processing Technology*, Vol. 137, pp. 10–16

Chowdhury, S.G., Srivastava, V.C., Ravikumar, B. & Soren, S. (2006a). *Scripta Materialia*, Vol. 54, pp. 1691–1696

Chowdhury, S.G., Dutta, A., Ravikumar, B. & Kumar, A. (2006b). *Materials Science and Engineering A*, Vol. 428, pp. 351–357

Costa, A.L.M., Reis, A.C.C., Kestens, L. & Andrade, M.S. (2005). *Materials Science and Engineering A*, Vol. 406, pp. 279–285

del Valle, J.A., Pérez-Prado, M.T. & Ruano, O.A. (2005). *Materials Science and Engineering A*, Vols. 410/411, pp. 353–357

Estrin, Y., Toth, L.S., Molinari, A. & Bréchet, Y. (1998). *Acta Materialia*, Vol. 46, pp. 5509–5522

Hansen, N. (2004). *Scripta Materialia*, Vol. 51, pp. 801–806

Heason, C.P. & Prangnell, P.B. (2002a). *Materials Science Forum*, Vols. 408–412, pp. 733– 738

Heason, C.P. & Prangnell, P.B. (2002b). *Proc. of Conference on Nanomaterials by Severe Plastic Deformation-NANOSPD2,*, Dec. 9-13, Vienna, Austria

Horita, Z., Smith, D.J., Furukawa, M., Nemoto, M., Valiev, R.Z. & Langdon, T.G. (1996). *Journal of Material Research*, Vol. 11, pp. 1880–1890

Huang, X., Tsuji, N., Hansen, N. & Minamino, Y. (2003). *Materials Science and Engineering A*, Vol. 340, pp. 265–271

Humphreys, F.J. & Hatherly, M. (2004). *Recrystallization and Related Annealing Phenomena*, Elsevier, Oxford

Kim, H.W., Kang, S.B., Xing, Z.P., Tsuji, N. & Minamino, Y. (2002). *Materials Science Forum*, Vols. 408–412, pp. 727–732

Kim, H.W., Kang, S.B., Tsuji, N. & Minamino, Y. (2005). *Metallurgical and Materials Transaction A*, Vol. 36, pp. 3151–3163

Kim, Y.S., Kang, S.H., & Shin, D.H. (2006). *Materials Science Forum,* Vols. 503/504, pp. 681–686

Kolahi, A., Akbarzadeh A. & Barnett, M.R. (2009). *Journal of Materials Processing Technology*, Vol. 209, pp. 1436-1444

Lee, S.H., Saito, Y., Sakai, T. & Utsunomiya, H. (2002). *Materials Science and Engineering A*, Vol. 325, pp. 228–235

Lee, S.H., Lee, C.H. & Lim, C.Y. (2004). *Materials Science Forum*, Vols. 449–452, pp. 161–164

Min, G., Lee, J.M., Kang, S.B. & Kim, H.W. (2006). *Materials. Letters*, Vol. 60, pp. 3255–3259

Mohebbi, M.S. (2009a). M.Sc. Thesis, Sharif University of Technology, Tehran, I.R. Iran

Mohebbi, M.S. & Akbarzadeh, A. (2009b). *Proc. of the 2nd Int. Conference on Ultrafine Grained and Nanostructured Materials (UFGNS2009)*, Nov. 14-15, Tehran University, Tehran, I.R. Iran

Mohebbi, M.S. & Akbarzadeh, A. (2010a). *Journal of Materials Processing Technology*, Vol. 210, pp. 510–517

Mohebbi, M.S. & Akbarzadeh, A. (2010b). *Materials Science and Engineering A*, Vol. 528, pp. 180–188

Mohebbi, M.S. & Akbarzadeh, A. (2010c). *Journal of Materials Processing Technology*, Vol. 210, pp. 389–395

Park, K.T., Kwon, H.J., Kim, W.J., & Kim, Y.S. (2001). *Materials Science Engineering A*, Vol. 316, pp. 145–152

Pérez-Prado, M.T., del Valle, J.A. & Ruano, O.A. (2004). *Scripta Materialia,* Vol. 51, pp. 1093–1097

Pirgazi H., Akbarzadeh, A., Petrov, R., Sidor, J. & Kestens, L. (2008a). *Materials Science and Engineering A*, Vol. 492, pp. 110–117

Pirgazi, H., Akbarzadeh, A., Petrov, R. & Kestens, L. (2008b). *Materials Science and Engineering A*, Vol. 497, pp. 132–138

Pirgazi, H. & Akbarzadeh, A. (2008c). *Proc. of the 2nd Conference on Nanostructures (NS2008)*, March 11-14, Kish University, Kish Island, I.R. Iran

Pirgazi, H. & Akbarzadeh, A. (2009). *Materials Science and Technology*, ol. 25, No. 5, pp. 625-631

Prangnell, P.B., Bowen, J.R. & Gholinia, A. (2001). *Proceedings of the 22nd Risø´ International Symposium on Materials Science*, pp. 105–126

Reis, A.C.C. & Kestens, L. (2005). *Solid State Phenomena*, Vol. 105, pp. 233–238

Reis, A.C.C. , Kestens, L. & Houbaert, Y. (2005). *Materials Science Forum*, Vols. 495–497, pp. 351–356

Richert, J. & Richert, M. (1986), *Aluminum*, Vol. 62, pp. 604–607

Rios, P. R. & Padilha, A. F. (2003). *Materials Research*, Vol. 6, No. 4, pp. 605–613

Ryazanov, A.I., Pavlov, S.A. & Kiritani, M. (2003). *Materials Science and Engineering A*, Vol. 350, pp. 245–250

Saito, Y., Utsunomiya, H., Tsuji, N. & Sakai, T (1999). *Acta Materialia*, Vol. 47, No. 2, pp. 579–583

Saito, Y., Tsuji, N., Utsunomiya, H., Sakai, T. & Hong, R.G. (1998). *Scripta Materialia*, Vol. 39, No. 9, pp. 1221–1227

Semiatin, S.L. & Jonas, J.J. (1984). *Formability and Workability of Metals*, American Society for Metals, Ohio, USA

Sevillano, J.G., Van Houtte, P. & Aernoudt, E. (1981). *Progress in Materials Science*, Vol. 25, pp. 69–134

Sherby, O.D. and Wadsworth, J. (2001). *Journal of Materials Processing Technology*, Vol. 117, pp. 347–353

Sponseller, D.L., Timmons, G.A. & Bakker, W. T. (1998). *Journal of Materials Engineering and Performance*, Vol. 7, No. 2, pp. 227-238

Takata, N., Okitsu, Y. & Tsuji, N. (2008). *J. Materials Science*, Vol. 43, pp. 7385–7390

Tsuji, N., Ueji, R. & Minamino, Y. (2002a). *Scripta Materialia*, Vol 47, pp. 69–76

Tsuji, N., Ito, Y., Saito, Y. & Minamino, Y. (2002b). *Scripta Materialia*, Vol. 47, pp. 893–899

Tsuji, N., Saito, Y., Lee, S.H. & Minamino, Y. (2003a). *Advanced Engineering Materials*, Vol. 5, No. 5, pp. 338–344

Tsuji, N., Toyoda, T., Minamino, Y., Koizumi, Y., Yamane, T., Komatsu, M. & Kiritani, M. (2003b). *Materials Science and Engineering A*, Vol. 350, pp. 108–116

Valiev, R.Z., Krasilnikov, N.A. & Tsenev, N.K. (1991). *Materials Science Forum Engineering A*, Vol. 137, pp. 35-41

Valiev, R.Z., Islamgaliev, R.K. & Alexandrov, I.V. (2000). *Progress in Materials Science*, Vol. 45, pp. 103–189

Van Houtte, P., Li, S.Y., Seefeldt, M. & Delannay, L. (2005). *International Journal of Plasticity*, Vol. 21, pp. 589–624

Van Houtte, P., Kanjarla, A.K., Van Bael, A., Seefeldt, M. & Delannay, L. (2006). *European Journal of Mechanics A-Solids*, Vol. 25, pp. 634–648

Wang, X., Li, P. & Wang, R. (2005). *Int. J. of Machine Tools Manufacture*, Vol. 45, pp. 373–378

Wang, Y.M. & Ma, E. (2004). *Materials Science and Engineering A*, Vols. 375–377, pp. 46–52

Wei, Q., Cheng, S., Ramesh, K.T. & Ma, E. (2004). *Materials Science and Engineering A*, Vol. 381, pp. 71–79

Wong, C.C., Dean, T.A. & Lin, J. (2003). *Int. J. of Machine Tools Manufacture*, Vol. 43, pp. 1419–1435

Zener, C. & Hollomon, J.H. (1944). J. Applied Physics, Vol. 15, pp. 22–32

Zhan, Z., He, Y., Wang, D. & Gao, W. (2006). *Surface and Coatings Technology*, Vol. 201, pp. 2684–2689
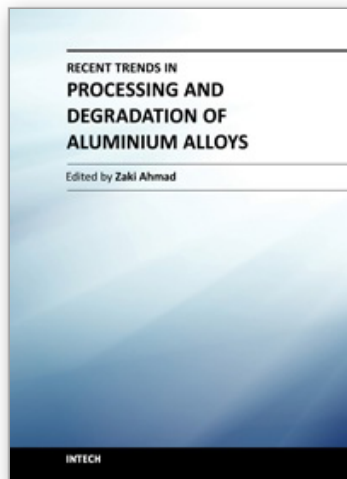
Recent Trends in Processing and Degradation of Aluminium Alloys

Edited by Prof. Zaki Ahmad

In the recent decade a quantum leap has been made in production of aluminum alloys and new techniques of casting, forming, welding and surface modification have been evolved to improve the structural integrity of aluminum alloys. This book covers the essential need for the industrial and academic communities for update information. It would also be useful for entrepreneurs technocrats and all those interested in the production and the application of aluminum alloys and strategic structures. It would also help the instructors at senior and graduate level to support their text.

How to reference

In order to correctly reference this scholarly work, feel free to copy and paste the following:

Abbas Akbarzadeh (2011). Nanostructure, Texture Evolution and Mechanical Properties of Aluminum Alloys Processed by Severe Plastic Deformation, Recent Trends in Processing and Degradation of Aluminium Alloys, Prof. Zaki Ahmad (Ed.), ISBN: 978-953-307-734-5, InTech, Available from:
http://www.intechopen.com/books/recent-trends-in-processing-and-degradation-of-aluminium-alloys/nanostructure-texture-evolution-and-mechanical-properties-of-aluminum-alloys-processed-by-severe-pla

INTECH

open science | open minds